

The osteogenic and angiogenic potential of microRNA-26a delivered via a non-viral delivery peptide for bone repair

Hannah Chambers ^a, Monika Ziminska ^a, Ahmed Elkashif ^a, Jordan Wilson ^a, John Redmond ^b, Antzele Tzagfiofli ^b, Cole Ferrefira ^j, Auden Baflouch ^j, Jasmfine Bogole ^j, Seth W. Donahue ^j, Nícholas J. Dunne ^{a,b,c,d,e,f,g,h,i,j}, * Heflen O. McCarthy ^a, *

^a School of Pharmacy, Queen's University Belfast, 97 Lisburn Road, Belfast BT9 7BL, UK

^b School of Mechanical and Manufacturing Engineering, Dublin City University, Dublin 9, Ireland

^c Biodesign Europe, Dublin City University, Dublin 9, Ireland

^d Centre for Medical Engineering Research, School of Mechanical and Manufacturing Engineering, Dublin City University, Dublin 9, Ireland

^e Department of Mechanical and Manufacturing Engineering, School of Engineering, Trinity College Dublin, Dublin 2, Ireland

^f Advanced Manufacturing Research Centre (AMBER), Royal College of Surgeons in Ireland and Trinity College Dublin, Dublin, Ireland

^g Advanced Materials and Bioengineering Research Centre (AMBER), Royal College of Surgeons in Ireland and Trinity College Dublin, Dublin, Ireland

^h Advanced Processing Technology Research Centre, Dublin City University, Dublin 9, Ireland

ⁱ Trinity Centre for Biomedical Engineering, Trinity Biomedical Sciences Institute, Trinity College Dublin, Dublin 2, Ireland

^j Department of Biomedical Engineering, University of Massachusetts, Amherst, United States

ARTICLE INFO

Keywords:

microRNA
DNA
miR26a
RALA peptide
Nanoparticle
Cardiac defect
Osteogenesis
Bone

ABSTRACT

Bone-related injuries and diseases are among the most common causes of morbidity worldwide. Current bone-regenerative strategies such as auto- and allografts are invasive by nature, with adverse effects such as pain, infection and donor site morbidity. MicroRNA (miRNA) gene therapy has emerged as a promising area of research, with miRNAs capable of regulating multiple gene pathways simultaneously through the repression of post-transcriptional mRNAs. miR-26a is a key regulator of osteogenesis and has been found to be upregulated following bone injury, where it induces osteodifferentiation of mesenchymal stem cells (MSCs) and facilitates bone formation. This study demonstrates, for the first time, that the amphipathic, cell-penetrating peptide RALA can efficiently deliver miR-26a to MSCs *in vitro* to regulate osteogenic signaling. Transfection with miR-26a significantly increased expression of osteogenic and angiogenic markers at both gene and protein levels. Using a rat cardiac defect model with a critical size defect, RALA/miR-26a NPs were delivered via an injectable, thermo-responsive Cs-g-PNIPAAm hydrogel to assess the impact on both rate and quality of bone healing. Critical defects treated with the RALA/miR-26a nanoparticles (NPs) had significantly increased bone volume and bone mineral density at 8 weeks, with increased blood vessel formation and mechanical properties. This study highlights the utility of RALA to deliver miR-26a for the purpose of bone healing with an injectable biomaterial, warranting further investigation of dose-related efficacy of the therapeutic across a range of *in vivo* models.

1. Introduction

Bone osteogenesis is a complex process that is closely regulated by signaling pathways of both committed and non-committed osteoprogenitor cells, resulting from the chemical stimuli of growth factors, cytokines and transcription factors [1]. MicroRNAs (miRNAs) regulate gene expression on a post-transcriptional level by binding to the target sequences in the 3' untranslated region (UTR) of one or more messenger RNA (mRNA) molecules [2]. This interaction results in translational

arrest or degradation by the RNA-induced silencing complex, leading to reduced production of cellular proteins. Inhibition of mRNA translation by miRNAs has emerged as an important regulator of developmental osteogenic signaling pathways, osteoblast growth and differentiation, osteoclast-mediated bone resorption activity, and bone homeostasis in the adult skeleton. Although miRNAs have a relatively fast decay, the regulation of existing mRNA and subsequent proteins can have longer-term effects [3]. Consequently, miRNAs can provide temporary, rapid tuning of gene expression. They are also involved in

* Corresponding authors at: School of Pharmacy, Queen's University Belfast, 97 Lisburn Road, Belfast BT9 7BL, UK.
E-mail address: h.mccarthy@qub.ac.uk (H.O. McCarthy).

osteoblast differentiation of mesenchymal stem cells (MSCs) through the regulation of Notch, transforming growth factor- β (TGF- β), bone morphogenic protein (BMP), tumour necrosis factor alpha (TNF- α), and Wnt/ β -catenin signalling pathways. This miRNA can either enhance or inhibit differentiation by binding to osteogenic transcription factors that include glycogen synthase kinase-3 beta (GSK3 β), Notch2, runt-related transcription factor 2 (RUNX2), and transforming growth factor beta (TGF- β) [4–6]. Furthermore, miRNAs have been identified as regulators of osteoblast and osteoclast behaviour, and are involved in the process of bone remodelling and multifaceted bone metabolic diseases such as osteoporosis [7].

Some miRNAs are downregulated during normal osteogenesis and, as a result, are considered as osteogenic inhibitors (miR-138, [8] 141, [9] 338 [10]); others are upregulated and are considered osteogenic promoters (miR-29b, [11] 196a, [12] 378 [13]). The literature on a selection of these miRNAs has revealed contradictory results, which suggests that a deeper understanding of the biological cues is required. For example, miR-29a can either inhibit or promote osteogenesis depending on the experimental conditions [14,15]. This exemplifies the inherent complexity of controlling several gene regulatory networks simultaneously, where there can be extensive crosstalk of the molecular mechanisms involved in osteogenic differentiation. Therefore, it is critical that an unintended biological consequences are considered when a miR therapy is selected for use in human patients.

The regulatory role of miR-26a in osteogenesis has been an area of much debate. Conflicting reports have been published on whether overexpression of miR-26a induces osteogenesis-inhibiting or osteogenesis-promoting effects. For example, Luzzi, et al. concluded that the presence of miR-26a had an inhibitory effect on the osteogenic differentiation of human adipose-derived stem cells (hADSCs). Conversely, inhibition of miR-26a by 2'-O-methyl-antisense RNA increased protein levels of SMAD1 transcription factor with enhanced osteodifferentiation [16]. Likewise, Li, et al. reported that overexpression of miR-26a inhibited osteodifferentiation of mouse ADSCs via direct targeting of the 3'UTR of Wnt5a, and subsequently downregulated the Wnt/Ca²⁺ signalling pathway [17].

However, miR-26a has also been reported to target GSK3 β to activate the Wnt/ β -catenin-signalling pathway which translocates β -catenin from the cytoplasm to the nucleus, thus enhancing its transcription [18,19]. GSK3 β is a negative regulator of osteogenesis via the attenuation of RUNX2 signalling [20]. MiR-26a binds to, and inhibits, GSK3 β to enhance osteogenesis through upregulation of RUNX2, the master regulator of osteoblastogenesis [21]. MiR-26a has also been shown to downregulate PTEN, which can lead to osteogenesis and improved vascularisation [22,23]. Specifically, when delivered *in vitro*, miR-26a regulates osteoblast function and promotes differentiation of MSCs into osteoblasts, supporting the use of this miRNA as a gene therapeutic for bone regeneration [22,24].

Reported target genes of miR-26a include SMAD1, GSK3 β and transducer of ERBB2 1 (Tob1); these modulate the expression of SMADs which are intracellular proteins responsible for the signalling transduction of the extracellular, transforming growth factor, beta (TGF- β) superfamily of ligands [25–27]. The TGF- β family of cytokines includes BMPs and growth differentiation factors (GDFs) such as GDF-2 and TGF- β s protein (TGF- β 1, TGF- β 2, and TGF- β 3). These have a fundamental role in coupling bone resorption and bone formation during postnatal bone homeostasis by binding to a cell-membrane bound type-II receptor, and by the subsequent recruitment and phosphorylation of a type-I receptor, which in turn phosphorylates receptor-regulated SMADs (R-SMADs) [28–30]. Therefore, miR-26a contributes to supporting osteogenesis and bone formation by targeting SMAD1-BMP signalling in bone-forming cells. miR-26a also plays a key role in vascular endothelial growth factor (VEGF)-mediated neovascularisation through direct targeting of Nogo-B receptor [31]. In *vitro* delivery of human bone MSCs (hBMSCs), transfected with 50 nM miR-26a mimics from a biodegradable heparin-hyaluronan-poly(ethylene glycol) diacrylate hydrogel, facilitated bone

regeneration along with increased vascularisation in a 5 mm calvarial mouse defect through osteogenesis-angiogenesis coupling [32]. Stimulation of the five network of blood vessels via angiogenesis is necessary for the conversion of hypertrophic cartilage template to bone during endochondral bone formation [33]. Additionally, sufficient angiogenesis, often controlled through VEGF signalling, is essential for adequate healing of fractures [34]. Osteogenic-angiogenic coupling is a commonly used approach for bone regeneration, and overcoming inadequacies in these signalling pathways through delivery of miR-26a may be an effective approach to improving bone healing [35].

MiR-26a is also significantly downregulated in fractures. Zou, et al. reported levels of miR-26a to be five times lower in patients with fractures compared to healthy volunteers [22]. Overexpression of miR-26a leads to: inhibition of osteoblast apoptosis and decrease of cell death; promotion of osteoblastic activity; formation of mineralised nodules through an increase in BMP-2 and WNT3a; and suppression of osteoclast formation by targeting connective tissue growth factor (CTGF) [22,36]. Weekly delivery of 15 μ g of miR-26a mimics, injected into the fracture site of femur periosteum for 8 weeks, promoted healing of a non-union fracture in a rat model by targeting SOSTDC1 and Wnt/ β -catenin signalling pathways [37]. This further supports claims that over-expression of miR-26a could promote osteogenesis.

Since the efficiency of any nucleic acid therapy is dependent on intracellular transport, a delivery system is required that protects the cargo from degradation, crosses the cell membrane, and escapes the endosome without evoking an immune response [38]. The amphiphatic fusogenic peptide RALA has been shown to complex anionic cargoes irrespective of size, protect the cargo from degradation, and escape endosomal environments ensuring release of the cargo into the cytoplasm [39–48]. This study reports for the first time on the use of RALA to deliver miR26a, in both DNA and miR mimics forms, from a thermoresponsive hydrogel for bone regeneration [49]. Studies were specifically designed to examine the physicochemical characteristics of the RALA/miR-26a nanoparticles, the osteogenic potential and gene targets in hBMSCs, the degradation profile of the hydrogel and the osteogenic and angiogenic potential in a rat critical-sized calvarial defect model.

2. Materials and methods

2.1. Materials

2.1.1. The RALA peptide

The RALA peptide was produced by solid state synthesis (fluoromethoxycarbonyl chemistry) (Biomatik, Canada) and supplied as a lyophilised powder that required reconstitution before use. Peptides were supplied in the acetate salt form and > 95% purity. Following cleavage from the resin, the desired products were purified and confirmed by Reverse Phase High Performance Liquid Chromatography (HPLC) using a 1260 Infinity II LC System (Agilent, USA).

2.1.2. Nucleic acids

pEGFP-N1 (Clontech, USA) and pcDNA3-miR26a2 (Addgene, UK) plasmids were purchased and subsequently propagated using MAX Efficiency® DH5 α ™ Competent Cells (Life Technologies, UK). Purification was completed using a PureLink® HiIPure Plasmid Filter Maxiprep Kit (Life Technologies, UK) and quantified by UV absorption at 260 nm using a Nanodrop (Thermo Fisher Scientific, UK). For the *in vivo* studies, a double-stranded miR-26a-5p mimic was delivered (Dharmacon, UK).

2.1.3. Cells

Human bone marrow-derived mesenchymal stem cells (hBMSCs) (Promocell, Germany) were used. Proliferation of the cell line was completed by the suppliers and was confirmed as *Mycoplasma*-free by monthly testing using the MycoAlert® Mycoplasma Detection Kit (Lonza, Switzerland).

2.1.4. *Anifmals*

Nine C57/BL6 mice used in the *in vivo* degradation study were housed in an open facility in Queen's University Belfast and experimental protocols were compliant with the UK Scientific Act 1986. Twenty-eight Wistar male rats used in the calvarial defect study were housed in the temperature-controlled animal care facility at the University of Massachusetts Amherst (USA). All housing and *in vivo* experimental procedures were performed in accordance with protocol #1815 approved by the Institutional Animal Care and Use Committee (IACUC) of the University of Massachusetts Amherst. Animals had *ad libitum* access to food and water during the experiment and were kept under standard day/night cycle.

2.2. Methods

2.2.1. *miR-26a gene target prediction*

In *silico* analysis of four publicly available bioinformatics algorithms – miRDB, TargetScan, miRTarBase and microcosm, [50,51] – were completed to identify the gene targets in which miR-26a is predicted to bind to the 3' UTR. The data were collated and arranged into a four-way Venn diagram. Target genes selected for further analysis, *i.e.* collagen Type 1 (COL1), RUNX2, osteocalcin (OCN), and vascular endothelial growth factor A (VEGF-A), were based on information available in the literature with regards to bone regeneration in hMSCs.

2.2.2. *Synthesis of NPs*

RALA/pmiR-26a and pDNA nanoparticles (NPs) self-assemble via electrostatic interactions under ambient temperatures. RALA/pDNA NPs were prepared at N:P ratios 1–15 by adding appropriate volumes of RALA peptide solution to 1 µg pDNA as previously described [39]. The NPs were incubated at ambient temperature for 30 min to allow the formation of the complexes. RALA/miR26a mimics NPs at N:P ratio of 8 were chosen for *in vivo* analysis (optimisation data not shown).

2.2.3. *NPs size and zeta potential analysis*

The mean hydrodynamic size of nanocomplexes synthesised using 1 µg of pmfR-26a dispersed in 50 µL of H₂O was determined using Dynamic Light Scattering at 20 °C with a Malvern Nano ZS (Malvern Instruments, UK). Mean surface charge (zeta potential) of the complexes was also measured by using Laser Doppler Velocimetry on the Malvern Nano ZS system.

2.2.4. *Encapsulation efficiency of miR-26a with the RALA peptide*

miR-26a NPs (1 µg of pmfR-26a) were formulated at various N:P ratios and added to a black 96-well microplate (Thermo Fisher Scientific, UK). 50 µL of Quant-iT™ PicoGreen® Reagent (Life Technologies, UK) diluted 1:200 in TAE 1× buffer was subsequently added to each well and incubated for 30 min at RT. Sample fluorescence was measured at 480/520 nm using a FLUOstar Omega microplate reader (BMG Labtech, Germany). Encapsulation efficiency was reported relative to a pmfR-26a-only control. Data are reported as the mean of three independent repeats ($n = 3, \pm \text{ SEM}$).

The complexation of pDNA by the RALA peptide was confirmed using Ion Exchange Chromatography (IEC). 0.5 g of the Ion Exchange Media, SP-Sephadex (Sigma-Aldrich, SPC25120, GER), was incubated in 10 mL of 1 M molecular biology grade NaCl (Sigma-Aldrich, Germany) overnight at room temperature to facilitate swelling of the column. After washing supernatant removal, the resin was washed three times using 10 mL Ultrapure water to ensure noionic solvent was present. 2 mL of washed resin was loaded into a filter column and packed under pressure. 20 µL of pmfR-26a or RALA/pmfR-26a NPs at ≥20 mg/mL concentration was loaded into the column and eluted with 3 mL of Ultrapure water. Finally, fractions were collected in 0.5 mL centrifuge tubes and analysed using a Nanodrop 2000 (Thermo Scientific, UK).

2.2.5. *Transfection studies in human BMSCs*

hBMSCs were seeded at a density of 30×10^3 cells into 24-well plates (Thermo Scientific, USA) 24 h prior to treatment. Once confluent, cells were conditioned for 2 h in Opti-MEM reduced serum media (Gibco, UK). Cells of the multi-dish were then supplemented with a treatment of RALA/pmfR-26a NPs, such that the total pmfR-26a in the well was 3.3 µg/cm², and RALA was 26.1 µg/cm². The following treatments were added to wells for comparative studies: (i) untreated control, (ii) RALA control (RALA/pEGFP-N1), with equivalent RALA used and (iii) RALA/pmfR-26a NPs. Following incubation for 4 h under standard culture conditions, the media was removed and replaced with serum-supplemented (10% FBS, 1% Pen/Strep) standard hMSC expansion media (XPAN). Cellular response was verified following post-transfection at weekly intervals. Osteogenic markers and predicted miR-26a targets were analysed by reverse transcription polymerase chain reaction (RT-PCR), hBMSCs were supplemented with osteoinduction media (Promocell, Germany) 72 h post-transfection, and a further negative control group of cells added that was cultured in standard growth media (no osteogenic induction) to determine primer specificity.

2.2.6. *Quantitative Real-Time PCR (qRT-PCR) for miR-26a expression from human BMSCs*

RNA was extracted from hBMSCs via phase separation using a miR-Vana isolation kit (Thermo Fisher Scientific, UK). Reverse transcription reactions for miR-26a and the endogenous control U6 spliceosomal RNA (U6) were completed according to the manufacturer's protocol (TaqMan Small RNA assay, Invitrogen, UK). Quantitative reverse transcription polymerase chain reaction (qRT-PCR) of miR-26a levels was performed using a Lightcycler 480 II (Roche, UK) according to the following parameters: 95 °C for 10 min (pre-incubation), then amplification via 40 cycles of 95 °C for 15 s, and 60 °C for 60 s. miR-26a expression was determined from the recorded Ct values using the ΔΔCT method, with gene expression reported as fold change compared to an untreated control, with U6 as the endogenous control.

2.2.7. *Flow cytometric analysis for GFP expression*

48 h post-transfection, hBMSCs transfected with RALA/pEGFP-N1 NPs were analysed for the presence of green fluorescent protein (GFP). GFP-expressing hBMSCs were detected using the fluorescence-activated cell sorting (FACS) cell sorter system (BD Biosciences, UK), and data were analysed using BD CellQuest™ Pro software. Results are reported as the mean of three independent repeats ($n = 3, \pm \text{ SEM}$).

2.2.8. *qRT-PCR analysis of miR-26a target genes*

For each of the target genes – COL1, RUNX2, OCN and VEGF-A – a specific primer set (forward and reverse, Table 1) was obtained from Integrated DNA Technologies, UK. qRT-PCR analysis was performed using a Lightcycler 480 II (Roche, UK) with the following cycling parameters: 95 °C for 5 min (pre-incubation), then amplification via 45 cycles of 95 °C for 10 s, 60 °C for 10 s, and 72 °C for 10 s. Gene expression was determined from the recorded Ct values using the ΔΔCT method, with gene expression reported as fold change compared to an untreated control, with glyceraldehyde-3-phosphate dehydrogenase (GAPDH) as an endogenous control.

2.2.9. *Immunofluorescence microscopy for late stage osteogenic markers in hBMSCs*

hBMSCs were plated on 13 mm coverslips (Agar Scientific, UK) and placed in a 24-well plate at a density of 30×10^3 cells per well. Following transfection with miR-26a NPs and culture in standard hMSC growth media (Promocell, Germany), cells were fixed using 4% paraformaldehyde (Sigma-Aldrich, UK) for 30 min at RT, washed with PBS, and blocked for 1 h using PBS containing 1% bovine serum albumin (Sigma-Aldrich, UK) and 0.01% Tween 20 (Sigma-Aldrich, UK). Cells were next incubated for 1 h at 37 °C with anti-osteocalcin (1:100, sc-

Table 1

Gene specific prfimer sets (Forward and Reverse).

Gene Target (NCBI Reference)	Description	Prfimer Sequence
COL1A1 (NM_000088.3)	<i>Homo sapiens</i> collagen type I alpha 1 chain	FWD 5' AAG AAC CCC AAG GAC
		AAG AG 3' 5' GTA GGT GAT GTT CTG
BGLAP (OCN) (NM_199173)	<i>Homo sapiens</i> bone gamma-carboxyglutamate protein (OCN)	REV GGA GG 3' 5' GGC AGC GAG GTA GTG
		FWD AAG AG 3' 5' CTC ACA CAC CTC CCT
RUNX2 (NM_001024630.3)	<i>Homo sapiens</i> RUNX2	REV CCT G 3' 5' GCG GTG CAA ACT TTC
		FWD TCC AG 3' 5' GAC TCT GTT GGT CTC
VEGF-A (NM_001025366.2)	<i>Homo sapiens</i> VEGF-A	REV GGT GG 3' 5' GAG CCT TGC TTT GCT
		FWD GCT CTA 3' 5' CAC CAG GGT CTC GAT
		REV TGG ATG 3'

21,742, Santa Cruz, USA) or anti-osteopontin (1:100, sc-73,464, Santa Cruz, USA) antibodies. Following washing in PBS, the primary antibody was incubated for 1 h at 37 °C with biotinylated horse anti-mouse Immunoglobulin G (IgG) secondary antibody (1:200, BA-2000, Vector Labs, UK). Membranes were washed three x 5 min with PBS, and incubated for 30 min at 4 °C with fluorescein streptavidin (1:200, SA-5001, Vector Labs, UK) as a fluorescent probe. Finally, coverslips were mounted on microscope slides (Agar Scientific, UK) with the use of DAPI-containing mounting media (ab104139, Abcam, UK) to visualize cells. Fluorescently stained cells were observed by immunofluorescence (IF) microscopy using a TSC SP5-Lefica Microsystems confocal microscope (Lefica, UK).

Images were analysed for normalized fluorescence using the imaging software Fiji 2.10.0 (an open-source extension of ImageJ) [52]. For cell counting, the 'Analyse Particles' macro was used on the images of DAPI-stained nuclei of cells, with a size filtering parameter of 200 pixels. For OCN and osteopontin (OPN) fluorescence intensity, the level of background fluorescence was set as a threshold parameter, and the mean fluorescence intensity of the image was determined. Each sample was imaged in three random locations per well, and reported values are the result of three independent experiments.

2.2.10. In-cell western assay for RALA/miR-26a effect on hBMSCs late-stage osteogenic markers

hBMSCs were plated in a 24-well plate at a density of 30 × 10³ cells per well. Following transfection with RALA/miR-26a NPs and culture in standard hMSC growth media (Promocell, Germany), treated and control cells were fixed using 4% paraformaldehyde (Sigma-Aldrich, UK) for 30 min. Cells were then permeabilized at 4 °C for 4 min by addition of 0.1% Triton X-100 (Sigma-Aldrich, UK) in PBS. For blocking, PBS/1% Marvel powder (Asda, UK) was added to the cells and left for 90 min on a shaker at 37 °C. After blocking, the cells were washed twice in 1% PBS, and cells were next incubated for 2 h at 37 °C with anti-osteocalcin (1:100, sc-21,742, Santa Cruz, USA) or anti-osteopontin (1:100, sc-73,464, Santa Cruz, USA) primary antibodies, alongside CellTag 700 (LI-COR Biosciences, UK) in a 1/500 dilution in PBS, for later analysis of the normalized distribution to cell number. After primary antibody incubation, cells were washed five times for 5 min on a shaker with wash buffer (PBS and 0.1% Tween 20). Following washing in PBS, the primary antibody was incubated for 1 h at 37 °C with biotinylated

horse anti-mouse IgG secondary antibody (1:10,000, BA-2000, Vector Labs, UK), washed, and incubated for 30 min with fluorescein streptavidin (1:200, SA-5001, Vector Labs, UK) as a fluorescent probe for the proteins of interest. The cells were washed, and antibody targets were detected in the 800-channel (green pseudo-colour), and normalized for cell number to the antibody signals from the 700-channel (red pseudo-colour) using an Odyssey Classic Infrared Cell Western (ICW) Assay Imaging System (LI-COR Biosciences, UK).

2.2.11. Mineralisation of hBMSCs: Affiliation red staining

To evaluate mineral deposition in hBMSCs transfected with miR-26a NPs, cells were washed with PBS and fixed for 30 min with 300 µL of 10% neutral buffered formalin (Sigma-Aldrich, UK). The cells were washed with distilled water and 300 µL of 40 mM, and pH 4.2 Alizarin red S (Sigma-Aldrich, UK) was added to the cell monolayer. Alizarin red staining solution was removed, and the cells were washed with distilled water to remove any unbound stain. Stained samples were air-dried, and microscopy images were captured using an EVOS XL inverted digital microscope (Thermo Fisher Scientific, UK). To quantify the degree of ARS staining, semi-quantitative analysis of the ARS was performed through extraction of the ARS dye using 100 mM cetylpyridinium chloride (CPC) (Sigma-Aldrich, UK) under gentle rocking for 30 min at ambient temperature. Finally, the absorbance of the CPC solution was read at 540 nm using a FLUOstar Omega microscope reader (BMG Labtech, Germany).

2.2.12. Fabrication of Cs-g-PNIPAAm hydrogel containing RALA/miR-26a NPs

The biodegradable and thermosensitive chitosan-grafted-poly(N-isopropylacrylamide) (Cs-g-PNIPAAm) hydrogel used to deliver RALA/miR-26a NPs *in vivo* was synthesized as previously described [49]. Briefly, the Cs-g-PNIPAAm hydrogel was synthesized through free radical polymerization by adding NIPAAm to 1% weight/volume Cs in acetic acid. The solution was purged for 1 h using dry nitrogen and polymerized by adding an initiator (ammonium persulfate, APS) and an accelerator (N,N,N,N-tetramethylethylene diamine, TEMED). The copolymer was dialysed for 5 days in double-distilled water at ambient temperature to remove any unreacted monomers and recovered by freeze-drying. To minimize the chances of pDNA integration into the genome [53], a miR-26a mimic was delivered instead of miR-26a for the *in vivo* application. The synthesized Cs-g-PNIPAAm copolymer was stabilized to 5% w/v concentration with RALA/miR-26a NPs for 18 h at 4 °C. The final miR-26a concentration in the hydrogel used for *in vivo* application was equivalent to 50 µg/mL. Therefore, 100 µL of each hydrogel containing 5 µg of miR-26a was injected into the caecal defect.

2.2.13. Scanning electron microscopy (SEM)

The synthesized hydrogel was solution in ultrapure water +/ RALA/miR-26a NPs to achieve a concentration of 50 µg/mL under agitation at 4 °C for 18 h. SEM imaging was conducted using a Hitachi TM3030 with a voltage of 15 kV.

2.2.14. Rheology

Rheological properties of the hydrogel were tested using a stress-controlled rheometer (model AR-2000ex) (TA Instruments, New Castle, DE, USA) with parallel plate geometry (40 mm diameter). The reconstituted hydrogel with a volume of 1.5 mL was used for the rheological analysis. G' and G" values were obtained by performing a temperature sweep at a frequency of 1 Hz over a range from 20 to 45 °C at a rate of 3 °C/min.

2.2.15. Hydrogel release

To determine RALA/miR-26a release, a volume of 100 µL hydrogel (corresponding to the 5 µg dose used *in vivo*) was incubated in the wells of a 24-well plate at 37 °C for 1 h to solubilize. Following this, 1.4 mL of

ultrapure water was added to each of the wells, and the plate was incubated at 37 °C. At predetermined time points, 50 µL of water was removed from each of the wells and stored at ambient temperature. RALA/miR-26a NPs were dissociated by adding 50 µL of 0.2 mg/mL Protease K (Sigma-Aldrich, UK) and incubating for 1 h at 37 °C. miRNA concentration was determined using a Quant-fit™ RiboGreen RNA Assay Kit by comparing to a standard curve produced with miR-26a at concentration range of 0.1–10 ng/µL (Thermo, USA). The percentage release of the 5 µg miRNA in each well was calculated at each time point.

miRNA-26a was detected from hydrogel release samples by RT-PCR. Samples were collected and digested as above and 5 µL was used for reverse transcription using the TaqMan™ MicroRNA Reverse Transcription Kit (Thermo Fisher, UK) followed by PCR using TaqMan™ MicroRNA Assays and TaqMan™ Universal Master Mix II, no UNG (Thermo Fisher, UK). PCR was conducted in a LightCycler 96 (Roche, UK) and analysed using the corresponding software.

2.2.16. Hydrogel degradation

To determine the *in vivo* degradation rate, 100 µL hydrogel with or without the incorporation of RALA NPs was weighed and injected subcutaneously into the flanks of C57BL/6 mice (N = 3 per group). Mice were sacrificed at various time points and the hydrogel was excised to determine the remaining mass. To stimulate *in vivo* degradation conditions, 100 µL hydrogel was incubated in the wells of a 24-well plate in PBS alone or PBS containing 3 mg/mL hyaluronidase. The plates were incubated for 8 weeks at 37 °C. The remaining mass of hydrogel within the wells was determined at various time points.

2.2.17. Caecal defect surgery

Crucifix-shaped caecal defect surgery was performed following a published protocol [54]. Wistar rats at 12 weeks were anaesthetised with isoflurane inhalation (2.5%–3.5%). Using a sterile technique, a 2–3 cm incision was made from the bridge of the nose to the back of the head. The skin and underlying periosteum were resected laterally using an elevator to expose the caecum. Using a surgical drill and trephine operating at 1500 RPM, a 6.8 mm diameter circular defect was made and removed in the parietal bone between the temporal line and the sagittal suture line. Although 8 mm defects are commonly used for crucifix-shaped cranial defects in rodents, diameters as low as 5 mm have been used when introducing two defects per animal, which reduces the number of animals needed and reduces the chance of interaction between adjacent defects [55–57]. Rats were randomised into treatment groups. For those receiving treatment, 100 µL volume of hydrogel was administered into the defect space directly after the defect was made. After treatment, the periosteum was stretched back over the skull into its original placement and sutured closed using 4/0 Maxon biodegradable sutures (Medtronic, USA). The skin over the periosteum was then sutured. The procedure ended with 3–6 BD autoclips (Fisher Scientific, USA) over the wound. Suture was used throughout the procedure.

Animals were monitored for signs of distress after surgery. No implant rejections or inflammatory reactions were observed in any of the surviving animals.

2.2.18. Micro-computed tomography analysis

Micro-Computed Tomography (µCT) analysis was performed *in vivo* at 4 and 8 weeks post-surgery. Animals were imaged using µCT (Bruker Skyscan 1276, USA) following anaesthesia with isoflurane inhalation. Animals were scanned using a voxel size of 40 µm and a 1 mm aluminum filter. The X-ray tube voltage was 60 kV, the current was 125 µA, and the exposure time was 490 ms. The 3D reconstructions were performed using NRecon v 2.0 (Bruker, USA). To assess bone regeneration in defects, a 6.8 mm diameter cylindrical volume of interest (VOI) overlaid the defect region to quantify bone volume (mm³) and bone mineral density (g/cm³) of new tissues.

2.2.19. Histological analysis

Following euthanasia via intracardiac exsanguination at 8 weeks post-surgery, caecal bones containing the defect region were harvested (n = 3 per group), fixed in 10% formalin for 72 h, and decalcified in formic acid overnight prior to histological examination. Each tissue section was embedded in paraffin, and 5 µm sections were cut from the approximate midline of the defect and positioned onto a glass microscope slide. Sections were stained with hematoxylin and eosin (H&E), and imaged at 400× magnification using a Keyence BZ-X800 light microscope (Keyence, Japan) fitted with a Nikon 40 × 0.6NA objective. Each imaged sample was scored on a 0–3 grading scale for presence of bone, blood vessels, and loose connective tissue. A score of 0 indicated no tissue in the defect, and a score of 3 indicated extensive tissue in the defect. All samples were graded independently relative to each other by two separate researchers.

2.2.20. Mechanical characterisation

Mechanical characterisation was completed to determine the maximum force, compressive strength, and the Young's modulus, for four representative caecal bone samples at both the defect and the natural bone sites on the opposite side of the parietal bone. Testing was performed using the Zwick Z005 testing machine (Zwick/Roell, Zwick Roell Ltd., UK), fitted with a 500 N load cell. Before mechanical characterisation, samples were preconditioned at 37 ± 0.5 °C for 1 ± 0.1 h. Testing was repeated at three different locations on the defect and the natural bone sites. Mechanical testing was performed in a hydrated environment, using a PBS-filled water bath maintained at 37 ± 0.5 °C. A pre-load of 0.2 N was first reached before the flat-faced cylindrical indenter (Ø1.1 mm) was used to apply the compressive loading at a rate of 2 mm/min, to either a maximum force of 20 N or fracture. The maximum force (F_{Max}) was recorded for each sample, and the compressive strength was calculated as the quotient of F_{Max} and the cross-sectional area of the bone defect site. The Young's modulus was calculated from the slope of the linear region of resulting stress vs. strain curves.

2.2.21. Statistical analysis

Unless otherwise stated, three independent experiments were completed for each analysis, and the results are presented as mean ± SEM, n = 3 (where n is equal to the number of independent batches prepared). Statistical analysis was performed using Prism 6.0 (GraphPad Software, USA). Statistical significance differences were then calculated using the two-way analysis of variance (2-way ANOVA), with a p-value of ≤0.05 considered significant: (*) p ≤ 0.05; (**) p ≤ 0.01; (***) p ≤ 0.001.

3. Results

3.1. Identification of miR-26a as a potential therapeutic target for osteogenesis

Multiple algorithms have been developed to computationally predict the human miR-mRNA interactions which help to identify the therapeutic targets of miRNAs. Four publicly available bioinformatic databases of miRNAs target genes have been used to identify overlapping targets of miR-26a (Fig. 1a) [50,51,58,59]. A four-way Venn diagram was constructed to determine the overlapping gene targets (Fig. 1a). The subsequent 26 predicted genes from the analysis, listed alongside with gene targets in red, were selected for further analysis, based on information available in the literature with regards to bone regeneration in hMSCs.

3.2. Characterisation of miR-26a NPs

ALA/miR-26a NPs were formulated with a N:P (representing molar ratio of positively-charged nitrogen atoms in the amino acid backbone to the negatively-charged phosphates in the nucleic acid

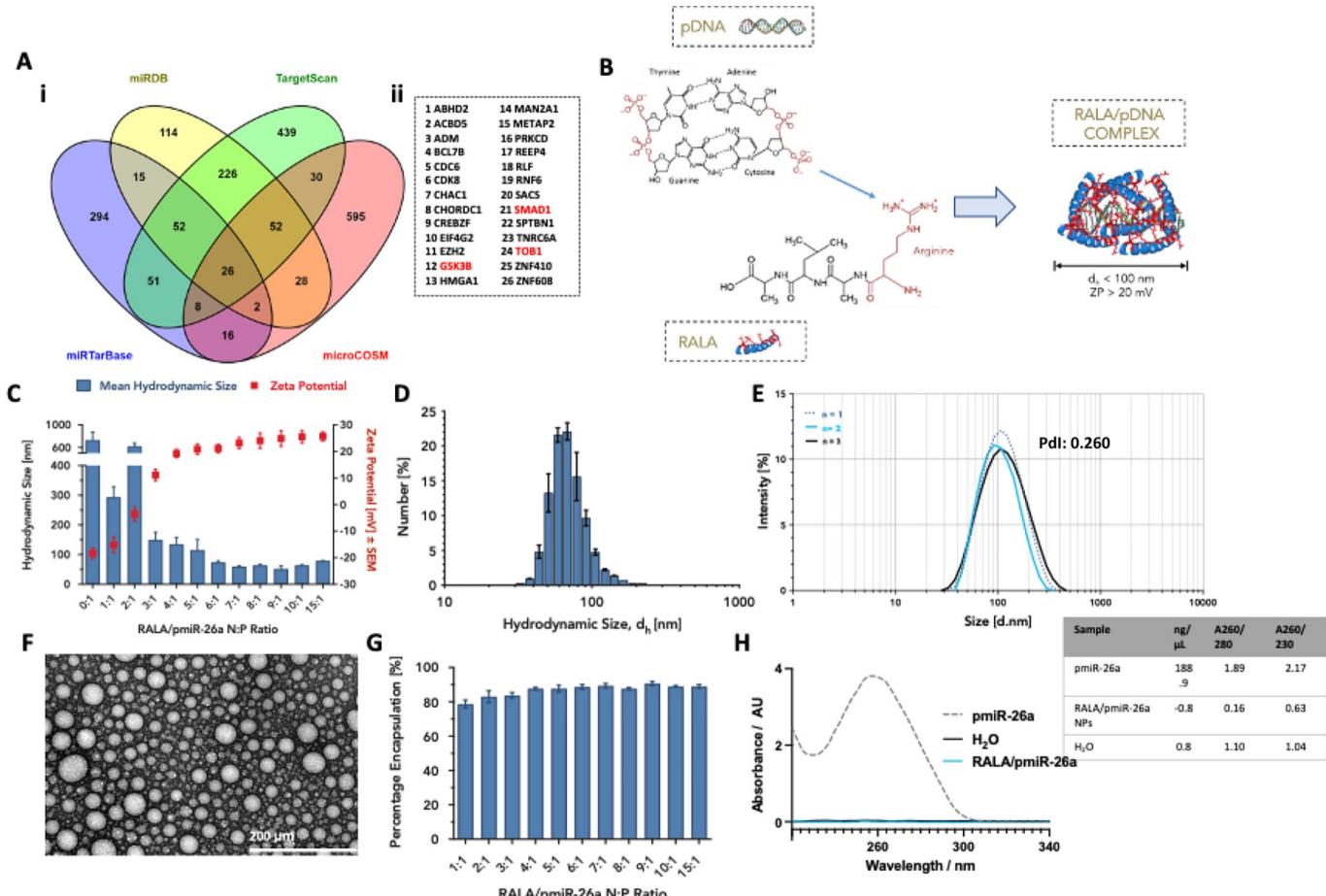


Fig. 1. Identification of gene targets of miR-26a with therapeutic potential and nanocomplex characterisation. A (if/ii) *In silico* bioinformatic predictions for the gene targets of miR-26a with genes of interest highlighted in red. B) RALA complexes with pmfR-26a via electrostatic interactions to form cationic nanosized particles ($< 100 \text{ nm}$). C) mean hydrodynamic size (d_h) and zeta potential (ZP) of pmfR-26a NPs at various RALA:pmfR-26a mass ratios 0–15. All measurements are reported as mean \pm SEM, ($n = 3$). D) Number-weighted size (d_h) distribution for pmfR-26a NPs at N:P 6. E) Corresponding representative size distribution by intensity of pmfR-26a NPs at N:P 6. F) TEM images revealing monodispersed, spherical RALA/pmfR-26a NPs at N:P 6. G) Encapsulation efficiency was quantified using Quant-iT™ PicoGreen reagent and measuring fluorescent output ($n = 3$). H) Ion Exchange Chromatography showing no free miR-26a when pmfR-26a NPs are run through the column ($n = 3$). (For interpretation of the references to colour in this figure legend, the reader is referred to the web version of this article.)

backbone) from 0 to 15. The mean hydrodynamic size (d_h) and zeta potential (ZP) of RALA/pmfR-26a NPs were determined to confirm the successful complexation and charge neutralisation of nucleic acid by the RALA peptide, and to create stable nanosized ($< 100 \text{ nm}$) particles. Size and charge of NPs are important factors for endocytosis, with only cationic particles with sizes $< 200 \text{ nm}$ entering cells via clathrin-mediated endocytosis [60]. Stable NPs [61] were formulated from N:P 6 upwards (Fig. 1c), whereas ratios below 6 showed either a negative, or a weak positive surface ZP, indicating unsuccessful complexation of the anionic nucleic acid. In addition to size and charge, the shape of nanocomplexes is an important factor that can determine the level of internalisation, as literature suggests that spherical NPs can be internalised at a rate as much as five-fold higher than rod-shaped nanocomplexes [62]. The spherical morphology of NPs at N:P 6 was confirmed on TEM micrographs (Fig. 1f) and with mean $d_h = 74 \pm 9 \text{ nm}$ and $ZP = +21.1 \pm 1.6 \text{ mV}$ (Fig. 1d and e). N:P 6 was selected for further analysis of the nanocomplexes.

To determine whether any free nucleic acid remained in solution following the addition of RALA, the complexation efficiency was assessed by Quant-iT™ PicoGreen™ assay and verified by IEC (N:P ratio 6). Results indicated that $> 85\%$ of miR-26a was encapsulated at N:P ratio 3 and above (Fig. 1g), with N:P 6 demonstrating an encapsulation efficiency of $88.7 \pm 1.5\%$. Full complexation of nucleic acid by RALA peptide was confirmed by IEC which showed no free pDNA when RALA/

pmfR-26a NPs were passed through the column (Fig. 1h).

3.3. Transfection of hBMSCs with miR-26a NPs

Following confirmation that RALA can effectively complex pmfR-26a into nanocomplexes, the maximum permissible dose of pmfR-26a that could be delivered to the cells without a significant cytotoxic effect was assessed (Fig. 2a). The maximum dose at N:P 6 was $1 \mu\text{g}$, equivalent to $3.3 \mu\text{g}$ of pmfR-26a per cm^2 with 70% confluent hBMSCs. The transfection efficiency was subsequently assessed *in vitro* using pEGFP-N1 as a reporter plasmid. GFP expression of transfected hBMSCs was found to be $27.9 \pm 2.2\%$ (Fig. 2b and c). To confirm that endogenous levels of miR-26a increase during osteogenesis, hBMSCs were subjected to osteodifferentiation by addition of the osteogenic media, with the levels of miR-26a quantified via qRT-PCR analysis (Fig. 2d). miR-26a expression continued to rise, reaching a 10.4 ± 1.5 -fold change by day 14. When the undifferentiated hBMSCs were transfected with RALA/pmfR26a, the expression of miR-26a increased 13.2 ± 2.4 -fold in relation to the untreated control at 48 h post-transfection (Fig. 2e). Taken together, these results coupled with the NP characterisation data, indicate that complexes at N:P 6 demonstrated a transfection efficiency that increased miR-26a levels without any significant compromise to the cell viability.

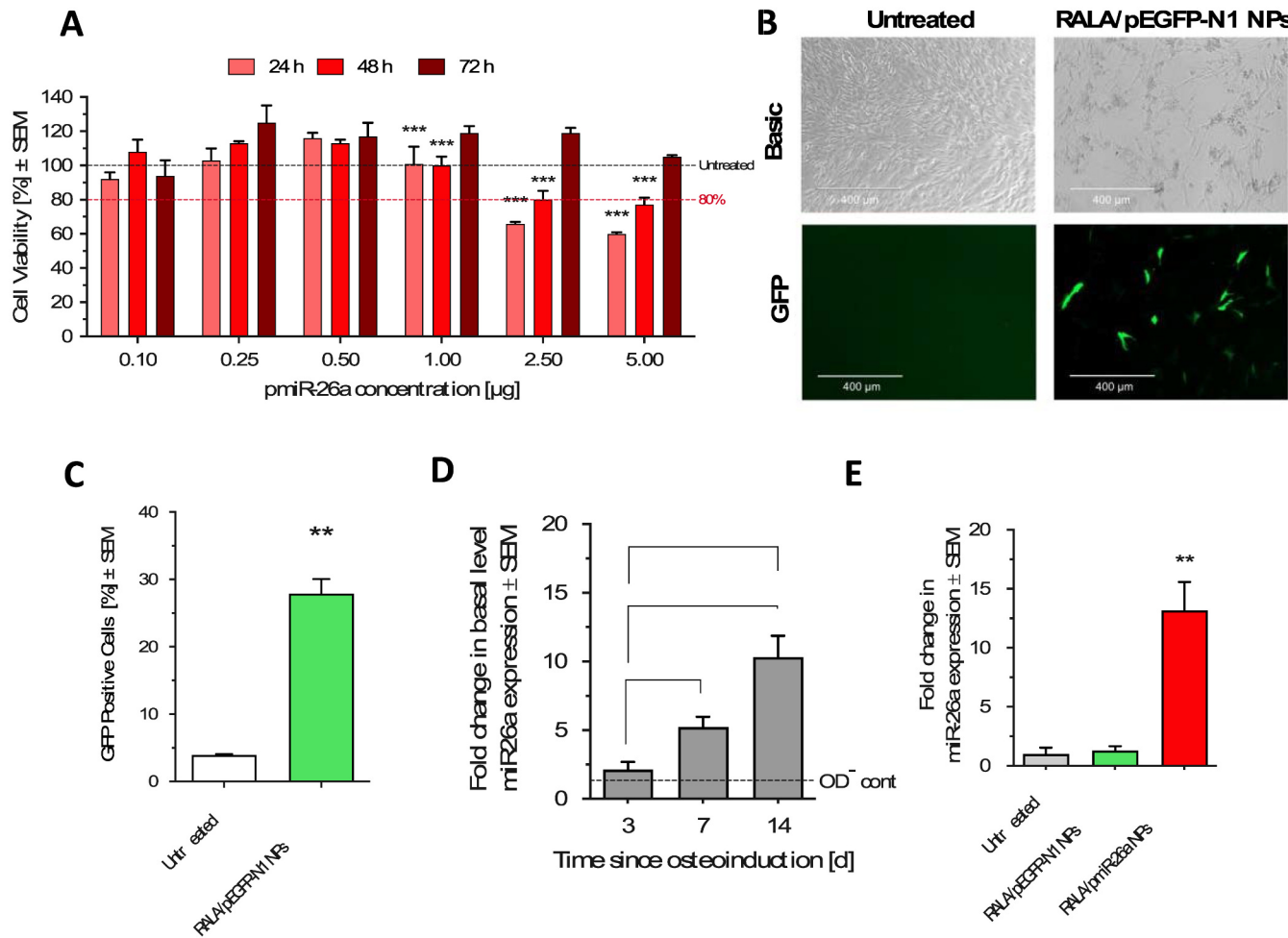


Fig. 2. Viability and transfection efficiency of RALA/nucleic acid nanocomplexes and analysis of miR-26a target gene protein levels post-transfection. A) hBMSCs were transfected with miR-26a NPs at a range of miRNA concentrations (0.1–5 µg/weffl). Cell viability was assessed using MTS assay at 24 h, 48 h and 72 h post-transfection. Cell viability was calculated as a measure of fluorescence relative to untreated cells. B) Fluorescent micrographs of GFP expression in hBMSCs 48 h post-transfection with RALA/pEGFP NPs. Reported images are representative of three independent repeats. C) Transfection efficiency was assessed 48 h later by flow cytometry for GFP positive cells ($n = 3, \pm \text{SEM}$). D) qRT-PCR analysis of miR-26a basal levels in hBMSCs at Day 3, 7 and 14 post-osteinduction. E) qRT-PCR analysis of miR-26a expression 48 h post-transfection with RALA/pEGFP-N1 NPs and RALA/pmiR-26a NPs in hBMSCs.

3.4. Determination of therapeutic effect of following overexpression of miR-26a in hBMSCs

Transfection of hBMSCs with RALA/pmiR-26a NPs subjected to osteodifferentiation induced the upregulation of osteogenic genes (Fig. 3a-c). COL1, RUNX2, OCN and VEGF-A were upregulated by Day 3. VEGF-A, an important growth factor for the osteogenic/angiogenic coupling of healthy bone regeneration, was significantly increased by Day 3, exhibiting a 1.7 ± 0.1 -fold change compared to untreated cells (Fig. 3d). OPN and OCN are osteogenic markers for the maturation stage of osteoprogenitor differentiation and late maturation/early mineralisation stage of osteoprogenitor differentiation, respectively. The protein levels of OPN and OCN in hBMSCs were examined at Day 21 and Day 28 with IF staining and confirmed with an In-Cel Western (ICW) assay. Intense positive staining of individual cells for OPN and OCN and a highly significant increase in normalized fluorescence were observed for miR-26a NPs transfected cells, exhibiting 17.0 ± 2.5 times more positive staining for OPN and 5.6 ± 1.4 times for OCN compared to the untreated control (Fig. 3e and g). ICW assay supported these findings, with the pmiR-26a NPs treatment group exhibiting a significant increase compared to control groups at day 21: an increase in OPN and OCN levels was reported as $50 \pm 10\%$ (Fig. 3f) and $40 \pm 9\%$ times greater than either of the control groups, respectively.

Delivery of pmiR-26a at a concentration of $3.3 \mu\text{g}/\text{cm}^2$ increased calcium deposition in hBMSCs by Day 7, as extensive staining was visible on both a macro- and micro-scale in the cells transfected with RALA/pmiR-26a NPs (Fig. 3f). The dissolved Alizarin Red S extracted from the cell culture monolayer provided a quantitative confirmation of the observed staining, exhibiting a $248 \pm 37\%$ increase in mineralisation in the RALA/pmiR-26a group compared to the untreated group of hBMSCs cultured in osteinduction media (Fig. 3j). Cells cultured in growth media showed a similar trend, with an increase in Alizarin Red S staining in the RALA/pmiR-26a NPs treated cells ($37 \pm 17\%$).

3.5. Hydrogel characterisation

The microstructure of the hydrogel with or without the addition of RALA/miR-26a NPs as determined by SEM imaging is presented in Fig. 4a. The hydrogel formed a meshed network with pores visible in the X1500 magnification image. Pore size ranged from 2 to $10 \mu\text{m}$. The addition of RALA NPs altered the structure of the hydrogel by reducing the number of pores visible in the structure. This is attributed to the presence of nanoparticles occupying the pores within the hydrogel.

The thermosensitive nature of the hydrogel with and without RALA/miR-26a NPs was confirmed through rheological analysis (Fig. 4b). For both hydrogel alone and hydrogel loaded with miR-26a NPs, at

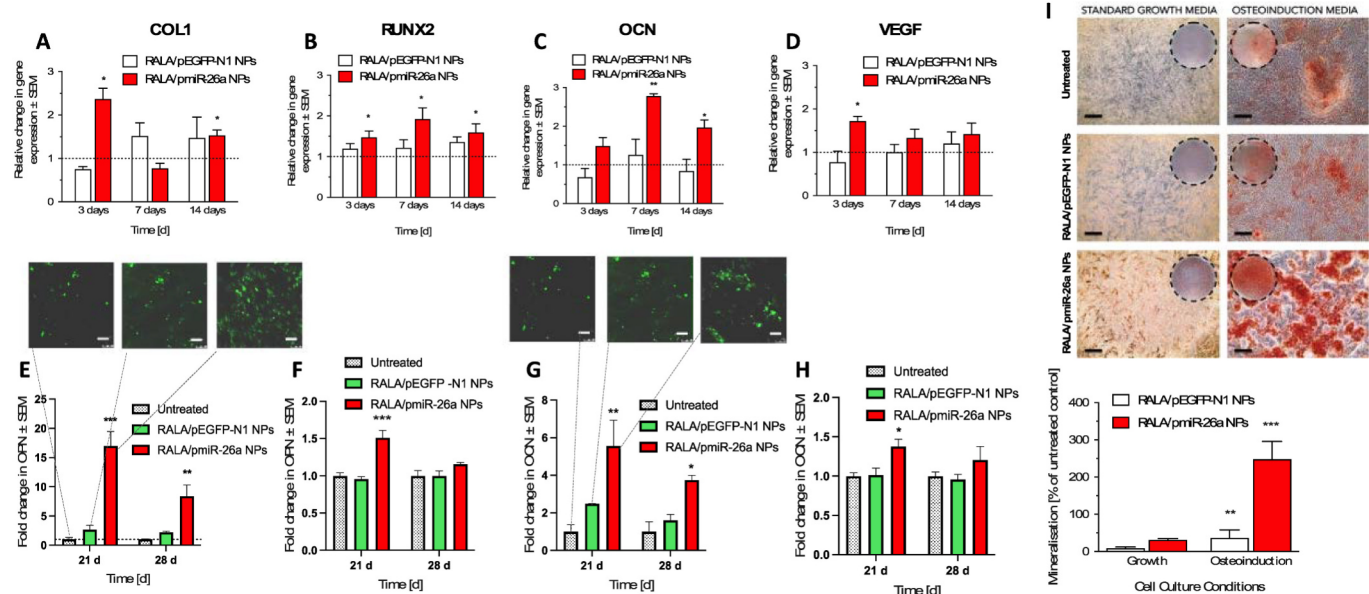


Fig. 3. Impact of miR-26a delivery on hBMSCs functionality. A-D) mRNA levels of target genes in hBMSCs post-transfection with pmfR-26a NPs. To quantify COL1, RUNX2, OCN and VEGF-A expression at Day 3, 7 and 14. Total RNA was reverse transcribed, and gene expression quantified relative to GAPDH as an endogenous control using qRT-PCR. Results are presented as relative fold change and reported as mean \pm SEM, $n = 3$. E) OPN IF quantification analysed at Day 21 and 28 post-transfection. Insets represent fluorescent micrographs with staining of osteopontin production (green) of untreated, RALA/pEGFP-N1 NPs-transfected, and RALA/pmiR-26a NPs-transfected hBMSCs following 21 days in culture (scale bars = 100 μ m). F) ICW assay to determine expression of OPN by hBMSCs at Day 21 and 28 post-transfection. G) OCN IF quantification as analysed at Day 21 and 28 post-transfection. Insets represent fluorescent micrographs with staining of osteopontin production (green) of untreated, RALA/pEGFP-N1 NPs transfected, and RALA/pmiR-26a NPs transfected hBMSCs following 21 days in culture (scale bars = 100 μ m). H) ICW assay to determine expression of OCN by hBMSCs at Day 21 and 28 post-transfection with RALA/pEGFP-N1 NPs and RALA/pmiR-26a NPs. I) Alizarin Red S staining of untreated hBMSCs, post-transfection with RALA/pEGFP-N1 NPs and RALA/pmiR-26a NPs, following 7 days in standard hMSC growth or osteoinduction media. Images are 4 \times microscopy images of a representative well from a 24-well microplate (scale bar = 500 μ m). J) Degree of alizarin red S staining, quantified via CPC extraction ($n = 3, \pm$ SEM). (For interpretation of the references to colour in this figure legend, the reader is referred to the web version of this article.)

temperatures >37 $^{\circ}$ C, the storage modulus (G') exceeds the loss modulus (G''), indicating a transition from a liquid to a solid state. The soft-gel transition temperature of the hydrogel was 32 $^{\circ}$ C which was unaffected by the addition of nanoparticles. At 37 $^{\circ}$ C, the G' of the hydrogel loaded with nanoparticles was higher (70.3 Pa) than the hydrogel alone (45.1 Pa), suggesting that the nanoparticles are supporting the structure of the hydrogel to form a polymer-network.

The release profile of the thermoresponsive hydrogel loaded with 50 μ g/mL RALA/miR-26a NPs was measured over the period of 1 week to confirm controlled release. In the first 8 h, there was an initial release of 1201.4 ng \pm 256 ng, which was maintained to 1243 ng \pm 197 ng at 24 h corresponding to 24% release (Fig. 4c). The consistent release observed between 8 and 24 h demonstrates that the hydrogel does control the release of miRNA. This initial release is attributed to swelling of the hydrogel and outward diffusion of the loaded nanoparticles. Further release beyond this point would be controlled *in vivo* through enzymatic degradation of the outer surface of the hydrogel, facilitating diffusion of nanoparticles located deeper in the hydrogel. Beyond 24 h, the measured miRNA concentration in solution appears to decrease, possibly due to the degradation of miRNA through hydrolysis. However, *in vivo*, the released NPs would be rapidly endocytosed and processed by cells, which should facilitate a sustained effect of the miR-26a as the hydrogel degrades over time.

The *in vivo* degradation study demonstrated that the hydrogel exhibited a steady degradation profile over 8 weeks (Fig. 4d). By 8 weeks post-injection, the proportion of hydrogel that had degraded was 84.83% and 86.08% for hydrogel alone and hydrogel loaded with RALA NPs respectively. *In vitro*, the hydrogel showed limited degradation in PBS only, with 13.28% degradation at 8 weeks. The addition of 3 mg/mL hyaluronate increased the degradation at 8 weeks to 60.22% and 83.31% for hydrogel only and hydrogel loaded with RALA NPs respectively, closely matching the *in vivo* degradation in the NP group. This provided

an accurate *in vitro* model for modelling *in vivo* degradation, where the release of NPs is controlled by passive diffusion mechanisms, coupled with ongoing enzymatic degradation via the protease of the hydrogel.

To assess whether the miRNA released from the *in vitro* incubation of the hydrogel is intact, samples containing released NPs were digested using proteinase K to release the encapsulated cargo. RT-PCR was used to detect miR-26a in the samples, revealing a fold change of 3398 in the presence of miR-26a in hydrogel samples loaded with the RALA/miR-26a NPs (Fig. 4e). This proved that the NPs released from the hydrogel contained intact and detectable miR-26a.

3.6. In vivo evaluation of RALA/miR-26a NPs in artificial size caecal defect in rats

All experimental animals recovered from the caecal defect surgery, and no adverse events were reported. Each rat was sacrificed 8 weeks post-surgery, and the caecal bone with the defect was harvested for analysis. H&E staining and assessment of the mechanical properties were conducted 8 weeks post-treatment, whereas µCT analysis was performed at 4 and 8 weeks to study the quantity and quality of the regenerated bone. The location of the defect is shown in Fig. 5a, and representative images of the rat's skull with the defect treated with thermosensitive hydrogel containing miR-26a NPs in Fig. 5b.

µCT scans demonstrated limited bone regeneration in the defect area in both groups after 4 weeks, which increased 8 weeks post-surgery (Fig. 5c). Bone formation initiated from the defect margins and progressed towards the centre as seen in the defect filled with hydrogel loaded with RALA/miR-26a NPs at week 8; bone formation was present along the defect margin and as connected islands of new bone in the centre of the defect. Although a trend for greater bone formation was observed in the defect filled with hydrogel loaded with miR-26a NPs compared to empty defect, no significant differences were observed

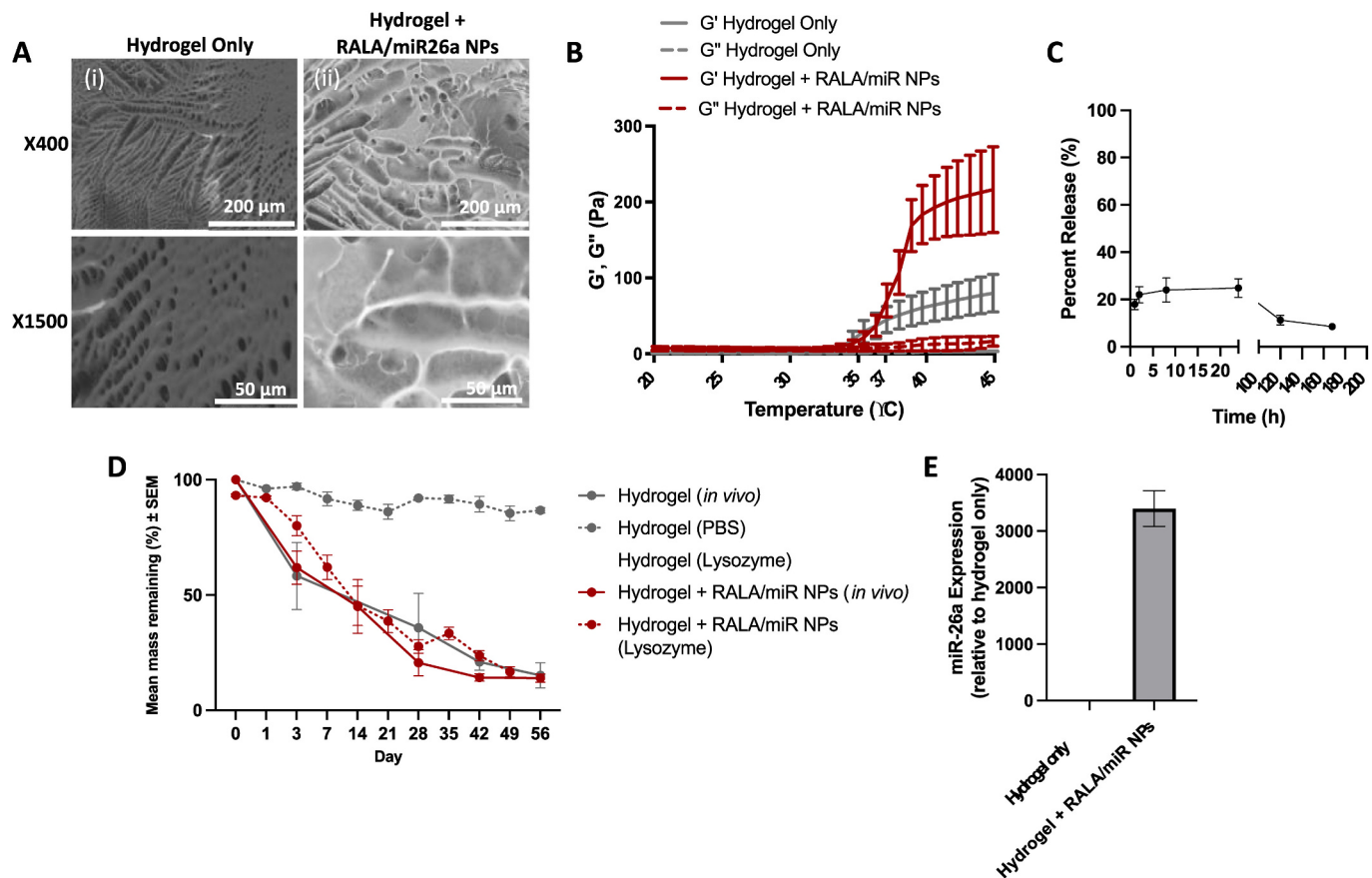


Fig. 4. A) SEM image of hydrogel at x400 and x1500 magnification as indicated. (i) Thermoresponsive hydrogel only (ii) Thermoresponsive hydrogel loaded with RALA/miR-26a NPs at a concentration of 50 ng/μL. B) Dynamic temperature sweep of the thermoresponsive hydrogel with or without the incorporation of RALA/miRNA NPs. C) Release of RALA/miRNA NPs from the thermoresponsive hydrogel incubated in ultrapure water at 37 °C over 7 days. D) *In vivo* degradation of the hydrogel measured by subcutaneous injection in C57BL/6 mice correlated with *in vitro* degradation determined by measuring mass of hydrogel over 8 weeks following incubation in PBS at 37 °C with or without 3 mg/mL lysozyme. E) RT-PCR showing fold change in miR-26a detected following incubation of hydrogel samples in ddH₂O for 3 days at 37 °C. All results are reported as mean ± SEM, n = 3.

between the groups at 4 and 8 weeks. However, sagittal *in vivo* μCT images (bottom row, Fig. 5c) revealed bone formation throughout the entire thickness of the calvarial defect, showing complete bridging at 8 weeks in 28.6% of empty defect and 71.4% of hydrogel loaded with RALA/miR-26a NPs group. Eight weeks post-surgery, bone volume and bone mineralised density, a major indicator of the quality and strength of the regenerated bone, [63] had increased in the RALA/miR-26a NPs treated defect compared to the empty defect by an average of 2.08 mm³ and 0.064 g/cm³, respectively (Fig. 5d and e). Furthermore, defects treated with RALA/miR-26a showed a statistically significant increase in bone volume and bone mineralised density at 8 weeks compared to 4 weeks. Although there was no statistically significant increase in bone formation and bone mineralised density between empty defect and hydrogel loaded with RALA/miR-26a NPs groups, the RALA/miR-26a NPs group showed considerably higher healing responses compared to untreated defect and smaller standard deviation of healing responses compared to the untreated control.

There was a non-significant increase in bone and vessel presence following treatment with hydrogel loaded with RALA/miR-26a NPs compared to the untreated control (Fig. 5f). In addition, the presence of loose connective tissue was less pronounced in miR-26a NPs-treated defects compared to the control. H&E slices revealed a similar trend to the μCT analysis, as the presence of normal bone formation was found within the defect area in both groups (Fig. 5h), with the defect width being smaller in the miR-26a group (1.26 ± 0.41 mm) compared to untreated control (3.09 ± 0.44 mm).

To determine the mechanical properties of the regenerated calvarial

bone, microindentation was used to measure the maximum load applied (force at bone defect fracture), compressive strength and Young's Modulus (Fig. 5g and h) [64]. Young's modulus, compressive strength and maximum force values recorded for the miR-26a-treated defect were higher in the miRNA-treated defects compared to the empty defect. Although these results were not significant, this indicates a trend towards improved mechanical performance of the regenerated bone region.

4. Discussion

miR-26a has emerged as a promising candidate for osteogenic gene therapy. However, the therapeutic use of miRNAs has been hampered by stability, high sensitivity for degradation in physiological conditions, and low cellular entry [65,66]. Successful use of miRNAs as therapeutics depends on the capabilities of vectors to protect the cargo and facilitate intracellular delivery. As well as having bone-regenerative effects, miR-26a has also been shown to be have an anti-tumour effect [67–69]. Due to the breadth of effects that miRNAs can have on both pathophysiological and therapeutic pathways, strategies for safe and efficient delivery to the site of action are essential. Use of the RALA peptide, as well as formulation into a thermoresponsive hydrogel, can protect the sensitive nucleic acid cargo and ensure its retention and gradual release to the intended site of action, avoiding off-target effects and uncontrollable miRNA release.

The data outlined in this study show for the first time how the miR-26a, delivered as nanoparticles using the 30-amino acid penetratin

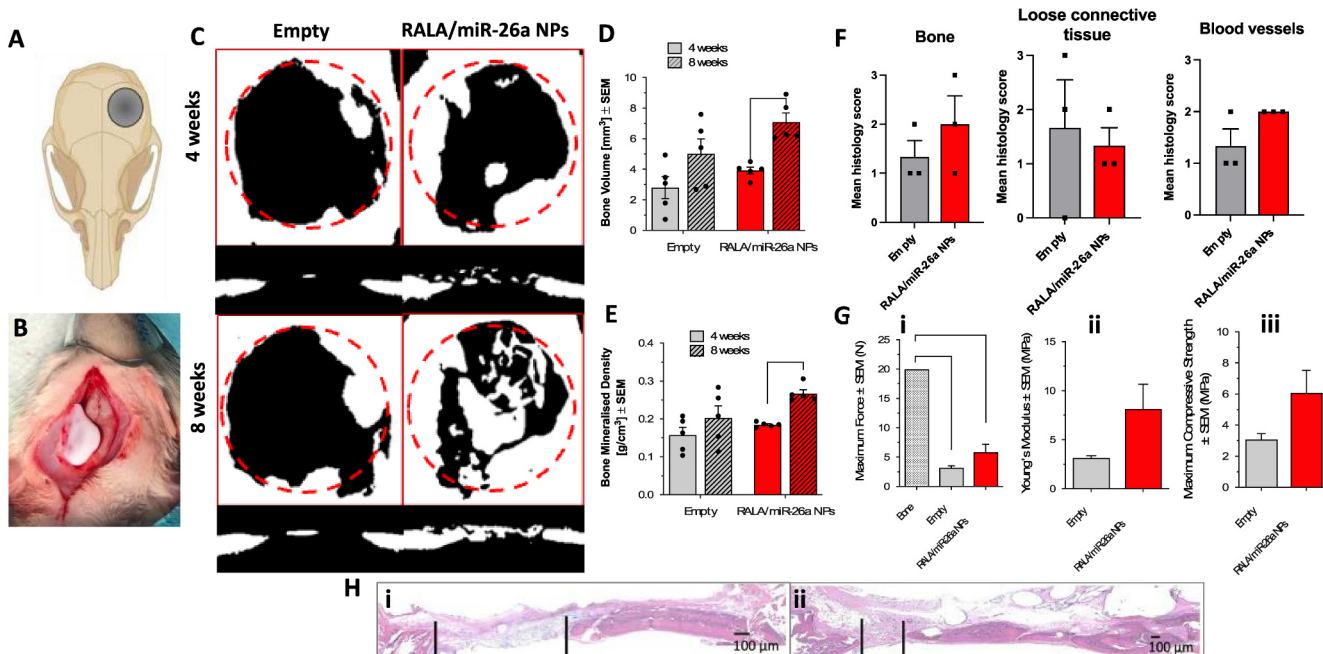


Fig. 5. *In vivo* delivery of RALA/miR-26a NPs *via* thermoresponsive and biodegradable hydrogel in a rat calvarial bone defect. A) Schematic representation of the location of the calvarial bone defect in rat. B) Representative image of 100 μ L of thermoresponsive hydrogel loaded with RALA/miR-26a NPs administered into the defect space. C) Representative coronal and sagittal μ CT scan images of bone within the defect region; white represents bone. D) Volume of bone within the region of interest at 8 weeks. E) Bone mineral density (g/cm^3) shown as an average density of all tissues within the region of interest at 8 weeks ($n = 5$, Mean \pm SEM). F) Presence of bone, loose connective tissue and blood vessels in calvarial cross-section slides stained with H&E from untreated control and RALA/miR-26a NPs group ($n = 3$) presented as score on a 0–3 grading scale. G) Mechanical properties: (i) Maximum Force, (ii) Young's Modulus, and (iii) Maximum compressive strength of empty defect area and defect filled with hydrogel loaded with RALA/miR-26a NPs ($n \geq 7$, Mean \pm SEM). H) Representative images of the calvarial cut on the transverse plane and stained with H&E. Black lines represent the distance between bone formation 8 weeks post-surgery in (i) empty defect and (ii) defect treated with miR-26a NPs delivered from a hydrogel. Magnification at 400 \times .

peptide RALA, can successfully increase bone regeneration. The delivery of miR-26a NPs exhibited significant increases in functionality *in vitro* in hBMSCs, demonstrated by osteogenic gene upregulation, increased production of OCN and OPN proteins, and deposition of mineralized tissue. Incorporation of miR-26a NPs into the thermoresponsive Cs-g-PNIPAAm hydrogel was also found to be an encouraging platform for a treatment of critical-sized calvarial defects in Wistar rats.

In agreement with the literature, the biofunctional analysis of miR-26a gene targets revealed that the BMP/SMAD, [70] GSK3 β and Wnt/β-catenin [71] pathways are among those regulated by miR-26a. It was demonstrated that the RALA/miR-26a formulation at a N:P ratio of 6 produced NPs with hydrodynamic size of ~74 nm, catonic in nature (exhibiting a net ZP of +21 mV), and with complete encapsulation. The physicochemical characteristics indicated that RALA/miR-26a nanocomplexes would be ideal for intracellular delivery *via* endocytic pathways [60], facilitating the subsequent nuclear transport of the pDNA to allow transcriptional processing for the intended increase in miR-26a *in vitro* and *in vivo*. The maximum tolerated dose of miR-26a was found to be 1 μ g, and it has previously been shown that this quantity is capable of eliciting an upregulation of the encoded gene in a range of cells in [46,72].

Using RALA/miR-26a NPs, a transfection efficiency of $27.9 \pm 2.2\%$ was obtained in hBMSCs. This was deemed as relatively high for primary hBMSCs, as primary cultured cells are known to be difficult to transfect. In fact, Madefira et al. showed a transfection efficiency of only 7% in isolated hBMSCs following lipofection with plasmid GFP [73]. The results presented in this study are comparable to a transfection efficiency of 24–36% reported by Cheung, et al. who used six commercial lipofection reagents and polymer reagents and GFP as a reporter gene to transfect hBMSCs [74]. In the present study, miR-26a expression was increased 13-fold, indicating successful delivery to the nucleus and subsequent transcription into functional endogenous miR-26a. Other

studies designed to deliver miR-26a into cells have shown mixed results. Transfection of immortalized cells typically yields high miR-26a upregulation of up to 1000-fold [75]. Zou et al. used a commercial lipofection reagent (X-tremeGENE) to deliver 50 nmol of miR-26a mimics into cultured osteoblast cells less than three-fold upregulation [22]. Zhang et al. reported 20–40-fold upregulation in miR-26a in primary mouse osteoblasts using self-assembled polyplexes with 60 pmol [66]. Yan et al. used mesoporous silica NPs to deliver a dose of 20 μ g/mL to produce a 2500-fold increase in miR26a in hBMSCs at 24 h [24]. There have been other innovative strategies, including the delivery of genetic cargo using exosomes to treat musculoskeletal disorders, which have received commercial transfection reagents in efficacy [76,77]. Despite the varied transfection efficiencies, this is the analysis of the downstream osteogenic effects in BMSCs that is critical. All of these studies reported similar levels of osteogenic gene expression, notably two-three-fold upregulation of COL1, RUNX2 and OCN. In the present study, similar downstream effects were achieved with a lower concentration of cargo (5 μ g/mL), indicating that RALA NP technology is more efficient in miR-26a delivery to BMSCs.

Increasing endogenous miR-26a levels *in vitro* led to a significant increase in COL1 mRNA as early as Day 3, indicating an increase in osteodifferentiation. Increased COL1 deposition by osteoblast cells has been shown to contribute to a feedback loop producing an increase in bone formation due to the cooperative nature of COL1 and non-collagenous proteins such as OCN, OPN, and bone sialoprotein. COL1 constitutes the basic framework of the extracellular matrix upon which these proteins are oriented prior to calcification [78,79]. Therefore, the increase in COL1 mRNA expression by Day 3, may also have a contributory effect on the appreciable increase in OCN mRNA observed at Day 7 and Day 14. Indeed, significant increases in RUNX2 and OCN mRNA levels were observed by Day 7, and remained significantly higher than untreated cells up to maturation stage (Day 14). This is in

agreement with results reported by Ifi et al. who demonstrated that hBMSCs transfected with miR-26a mimics, had elevated mRNA levels for BMP2, OCN, COL1 and RUNX2 by Day 2, remaining up to 14 days [80]. Additionally, both Wang et al. and Su et al. showed significant increases in OCN and RUNX2 mRNA levels after 48 h by increasing the endogenous level of miR-26a in murine BMSCs [26,81].

The downstream effect of miR-26a NPs on the expression of angiogenic growth factor VEGF was investigated with respect to osteodifferentiation. Bone angiogenesis is necessary for transport of oxygen and nutrients, recruitment of MSCs and osteoblasts in the early stage during osteogenesis, and in the later stage, for trabecular bone formation and maturation [82]. Following transfection with miR-26a NPs, a short-term upregulation of VEGF-A mRNA expression was observed, as human BMSCs exhibited a two-fold increase in VEGF-A at Day 3 with expression levels returning to control levels before Day 7. Increased levels of VEGF-A are present in the hematoma that forms post-fracture indicating its importance in fracture repair. [83] This early influx of VEGF-A mediates the progression of the bone healing process and has been shown to be expressed highly during the early stages of osteodifferentiation (< 7 days) in hMSCs. [84]

NP delivery of miR-26a had a positive effect on the production of OPN and OCN - important osteoblastic phenotype protein markers, and on mineralisation. Protein production of both OPN and OCN was significantly increased 21 days post-transfection. Deposition of calcium phosphate by MSCs undergoing osteogenic differentiation is indicative of matrix maturation and is routinely used as an important marker for successful bone regeneration [85]. Enhanced mineral deposition in the transfected hBMSCs was determined through the presence of Alizarin red staining, and semi-quantitatively measured via extraction. The difference between the treatments was most enhanced when the cells were under the influence of forced osteodifferentiation, where positive staining for mineralisation was enhanced by 248% in miR-26a NPs transfected cells. This finding clearly indicates that by "priming" hBMSCs via miR-26a NPs transfection, the rate and extent of osteodifferentiation can be significantly enhanced. Interestingly, an increase of 31% in mineralisation was observed in the GFP NPs transfected cells. RALA/pEGFP-N1 appears to exhibit a moderate amount of bioactivity with respect to increasing osteogenesis, most apparent when used in conjunction with osteoinductive media. The influence of cell-penetrating peptides on stress fibre formation and focal adhesions of MSCs are potentially responsible for this moderate therapeutic outcome [86,87].

The therapeutic potential of the RALA/miR-26a NPs loaded into a thermoresponsive hydrogel was evaluated *in vivo* in a rat critical-sized calvarial defect model. This hydrogel has been extensively characterised in a previous study, where it was shown that the hydrogel could be formulated through free radical polymerisation and showed thermoresponsive and degradation capabilities which could be tailored by altering the formulation [49]. The microstructure and degradation of the hydrogel, as well as protection of miRNA by RALA NPs following release was confirmed in the current study. The delivery system was capable of releasing nanoparticles containing intact miRNA in a controlled manner, while exhibiting a degradation profile suitable for the timeframe required for the healing of large bone defects.

The miR-26a NPs containing a total of 5 µg of miR from a thermoresponsive hydrogel accelerated the repair of the critical-size calvarial defect in Wistar rats. The biodegradable Cs-g-PNIPAAm hydrogel developed by our group was utilised here as an injectable biomaterial for the miR-26a NPs [49]. The hydrogel is well characterised and was formulated to degrade gradually over a period of 8 weeks, delivering functional RALA/miR NPs to the surrounding cells. In this study, bone volume in the miR-26a-treated groups increased on average by 39.8% and 41.5% at 4 and 8 weeks respectively, compared to the empty defect. Bone-mineralised density increased by 17.2% and 31.6% at 4 and 8 weeks respectively. The miR-26a NP group also demonstrated improved mechanical properties when compared to the untreated defect at Week

8, which was indicative of newly regenerated bone within the defect site. Morphology of the new bone was evaluated through H&E-stained transverse sections cut in the approximate centre of defects. Slices showed compact bone matrix, and the bridging was observed in 3 out of 5 animals with the 6.8 mm diameter circular defect. The angiogenic effect of miR-26a through VEGF modulation observed *in vitro* was confirmed *in vivo*, as indicated by a 40% increase in new vessel formation in the miR-26a group. These results indicate that miR-26a is successfully delivered to the MSCs present within the defect which then stimulates osteogenic and angiogenic signalling and bone healing.

The majority of *in vivo* studies exploring miR-26a therapy for bone regeneration are based on transfected stem cells [80,88,89]. Downstream clinical translation of such approaches might be unfeasible due to recognised limitations associated with stem cell therapies (invasive harvesting techniques, immunogenicity, and limited survival *in vivo*) [90]. Direct miR-26a delivery has been shown to improve bone regeneration in *in vivo* mouse models [66]. Ifi et al. reported approximately 30% increase in bone volume following treatment with miR-26a compared to negative control [91]. Sun et al. reported new bone formation observed in a non-union rat femur model when 15 µg of miR-26a mimic was delivered weekly for 8 weeks (total of 120 µg of miR per animal) [37]. The present study demonstrates a noticeable improvement in osteogenic and angiogenic potential in *vitro* with a RALA/miR-26a loaded hydrogel containing a total of 5 µg of the nucleic acid. This approach protects the miRNA and facilitates cellular delivery, thus exhibiting similar therapeutic effects at a considerably lower dose. Future studies will focus on assessment of bone regeneration in critical-sized bone defect models when a higher dose of up to 20 µg is delivered. The osteogenic potential of miR-26a delivered via a NP-loaded scaffold has also been shown *in vivo*, with a 62.2% increase in bone volume observed 4 weeks after implantation [92]. However, one of the major drawbacks of current bone-regenerative techniques is the invasive nature of the intervention. While scaffolds can be useful carriers of gene therapy vectors, injectable therapies such as the hydrogel presented in this study present a safe and non-invasive method of delivery for the therapeutic.

In summary, miR-26a has been identified as an important miRNA, regulating osteodifferentiation of hBMSCs. miR-26a levels increased significantly in hBMSCs undergoing the phenotypic change to mature osteoblasts. The amphipathic peptide RALA was capable of condensing miR-26a nucleic acid into nanosized (<150 nm) particles for increased transfection of hBMSCs, leading to a significant overexpression of miR-26a *in vitro*. Such levels of miR-26a significantly increased osteogenic markers on both a genomic and proteomic level, leading to accelerated mineralisation of hBMSCs and a short-term increase in the mRNA levels of the angiogenic factor VEGF. Furthermore, *in vivo* results demonstrated that a hydrogel loaded with 5 µg of miR-26a can effectively enhance bone healing.

CRediT authorship contribution statement

Phillip Chambers: Writing – original draft, Methodology, Investigation, Data curation. **Monika Ziminska:** Writing – original draft, Methodology, Investigation, Data curation. **Ahmed Elkashif:** Writing – review & editing, Methodology, Investigation, Formal analysis. **Jordan Wilson:** Writing – review & editing, Methodology, Investigation. **John Redmond:** Methodology, Investigation, Formal analysis, Data curation. **Antzela Tzagiollari:** Methodology, Investigation, Formal analysis. **Cole Ferreira:** Writing – review & editing, Methodology, Investigation, Formal analysis. **Auden Balouch:** Writing – review & editing, Methodology, Investigation, Formal analysis. **Jasmine Bogle:** Writing – review & editing, Methodology, Investigation, Formal analysis. **Seth W. Donahue:** Writing – review & editing, Project administration, Methodology, Investigation, Formal analysis. **Nicholas J. Dunne:** Writing – review & editing, Supervision, Resources, Project administration, Formal analysis, Conceptualization. **Helen O. McCarthy:** Writing –

review & editing, Writing – original draft, Visualization, Supervision, Resources, Project administration, Funding acquisition, Conceptualization.

Data availability

Data will be made available on request.

Acknowledgements

Evan Dempsey and Parisa Ruschke for help with animal handling and surgical procedures, Aladdin Mohammed for assistance with analysing the micro-computed tomography scans, the National Science Foundation for funding (Award 1854387) and US-Ireland Grant 044.

References

- G. Hutchings, L. Moncrieff, C. Dompe, K. Janowicz, R. Sibbick, A. Bryja, et al., Bone regeneration, reconstruction and use of osteogenic cells from basic knowledge, animal models to clinical trials, *J. Clin. Med.* 9 (1) (2020 Jan 1) 139.
- J. O'Brien, H. Hayder, Y. Zayed, C. Peng, Overview of microRNA biogenesis, mechanisms of actions, and circuation, *Front. Endocrinol. (Lausanne)* 9 (AUG (2018 Aug 3) 402.
- M.J. Marzfi, F. Ghafri, B. Cerruti, S. De Pretto, P. Bonetti, C. Giacometti, et al., Degradation dynamics of microRNAs revealed by a novel pulse-chase approach, *Genome Res.* 26 (4) (2016 Apr 1) 554.
- I. Tiforecu, V. Pruna, V.V. Jfinga, M. Sfimionescu, Osteoblast ontogeny and implications for bone pathology: an overview, *Cell Tissue Res.* 355 (1) (2014 Jan 23–33).
- Y. Ili, L. Fan, S. Lfui, W. Lfui, H. Zhang, T. Zhou, et al., The promotion of bone regeneration through positive regulation of angiogenic-osteogenic coupling using microRNA-26a, *Biomaterials*. 34 (21) (2013 Jul) 5048–5058.
- Z. Lfui, M.Q. Hassan, M. Jafferji, R.I. Aqeilan, R. Garzon, C.M. Croce, et al., Biological functions of miR-29b contribute to positive regulation of osteoblast differentiation, *J. Biol. Chem.* 284 (23) (2009 Jun 5) 15676–15684.
- A.J. Van Wijnen, J. Van De Peppel, J.P. Van Leeuwen, J.B. Lfian, G.S. Stefin, J. J. Westendorp, et al., MicroRNA functions in osteogenesis and dysfunctions in osteoporosis, *Curr. Osteoporos. Rep.* 11 (2) (2013 Jun) 72–82.
- H. Zheng, D. Ramnarain, B.A. Anderson, E. Tycksen, R. Nunfley, A. McAuliffe, MicroRNA-138 inhibits osteogenic differentiation and mineralization of human dedifferentiated chondrocytes by regulating RhoC and the actin cytoskeleton, *JBMR Plus*. 3 (2) (2019 Feb 1).
- F. Xue, J. Wu, W. Feng, T. Hao, Y. Lfui, W. Wang, MicroRNA-141 inhibits the differentiation of bone marrow-derived mesenchymal stem cells in steroid-induced osteocrosis via EZF3, *Mol. Med. Rep.* 26 (1) (2022 Jul 1).
- H. Lfui, Q. Sun, C. Wan, L. Ili, L. Zhang, Z. Chen, MicroRNA-338-3p regulates osteogenic differentiation of mouse bone marrow stromal stem cells by targeting Runx2 and Fgfr2, *J. Cell. Physiol.* 229 (10) (2014) 1494–1502.
- T. Pan, W. Song, H. Gao, T. Ili, X. Cao, S. Zhong, et al., miR-29b-loaded gold nanoparticles targeting to the endoplasmic reticulum for synergistic promotion of osteogenic differentiation, *ACS Appl. Mater. Interfaces* 8 (30) (2016 Aug 3) 1917–1922.
- G. Ili, M. Meng, L. Wang, X. Shao, Y. Ili, J. Cheng, et al., microRNA-19a promotes osteogenic differentiation and inhibits adipogenic differentiation of adipose stem cells via regulating β -catenin pathway, *Am. J. Transl. Res.* 11 (5) (2019) 3081.
- M. Hupkes, A.M. Sotoca, J.M. Hendriks, E.J. van Zoelen, K.J. Decherling, MicroRNA miR-378 promotes BMP2-induced osteogenic differentiation of mesenchymal progenitor cells, *BMC Mol. Biol.* 15 (2014 Jan 27) 1.
- K. Tan, Y.T. Peng, P. Guo, MicroRNA-29a promotes osteogenic differentiation of mesenchymal stem cells via targeting HDAC4, *Eur. Rev. Med. Pharmacol. Sci.* 22 (11) (2018) 3318–3326.
- C. Wang, M. Zhu, D. Yang, X. Hu, X. Wen, A. Lfui, MicroRNA-29a-3p inhibits proliferation and osteogenic differentiation of human bone marrow mesenchymal stem cells via targeting FOXO3 and repressing Wnt/ β -catenin signalling in steroid-associated osteocrosis, *Int. J. Stem Cells* 15 (3) (2022 Aug 1) 324–333.
- E. Lufi, F. Marfini, S.C. Saha, I. Tognarini, G. Gaffi, M.L. Brandi, Osteogenic differentiation of human adipose tissue-derived stem cells is modulated by the miR-26a targeting of the SMAD1 transcription factor, *J. Bone Miner. Res.* 23 (2) (2008 Feb 1) 287–295.
- S. Ili, C. Hu, J. Ili, L. Lfui, W. Jfing, W. Tang, et al., Effect of miR-26a-5p on the Wnt/Ca²⁺ pathway and osteogenic differentiation of mouse adipose-derived mesenchymal stem cells, *Cellul. Tissue Int.* 99 (2) (2016 Aug 1) 174–186.
- E. Lufi, F. Marfini, I. Tognarini, G. Gaffi, A. Falchetti, M.L. Brandi, The regulatory network Menin-MicroRNA 26a as a possible target for RNA-based therapy of bone diseases. <https://home.fliebertpub.com/nat>.
- R. Ili, H. Wang, J.V. John, H. Song, M.J. Teusink, J. Xie, 3D hybrid nanofiber aerogels combining with nanoparticles made of a biodegradable and targeting polycation and MiR-26a for bone repair, *Adv. Funct. Mater.* 30 (49) (2020 Dec 1) 2005531.
- F. Kugimiyama, H. Kawaguchi, S. Ohba, N. Kawamura, M. Hirata, H. Chikuda, et al., GSK-3 β controls osteogenesis through regulating Runx2 activity, *PLoS One* 2 (9) (2007 Sep 5).
- H. Wu, T.W. Whittfield, J.A.R. Gordon, J.R. Dobson, P.W.L. Taf, A.J. van Wijnen, et al., Genomic occupancy of Runx2 with global expression profiling identifies a novel dimension to control of osteoblastogenesis, *Genome Biol.* 15 (3) (2014 Mar 21) 1–17.
- J. Zou, J. Sun, H. Chen, X. Fan, Z. Qian, Y. Ili, et al., The regulatory roles of miR-26a in the development of fracture and osteoblasts, *Ann. Transl. Med.* 10 (2) (2022 Jan) 37.
- Y. Chen, H. Yu, D. Zhu, P. Lfui, J. Yfui, D. Lfui, et al., miR-136-3p targets PTEN to regulate vascularization and bone formation and ameliorates alcohol-induced osteopenia, *FASEB J.* 34 (4) (2020 Apr 1) 5348–5362.
- J. Yan, X. Lu, X. Zhu, X. Hu, L. Wang, J. Qian, et al., Effects of miR-26a on osteogenic differentiation of bone marrow mesenchymal stem cells by a mesoporous silica nanoparticle - PEI - peptide system, *Int. J. Nanomedicine* 15 (2020) 497.
- E. Lufi, F. Marfini, I. Tognarini, G. Gaffi, A. Falchetti, M.L. Brandi, The regulatory network menin-microRNA 26a as a possible target for RNA-based therapy of bone diseases, *Nucl. Acid Ther.* 22 (2) (2012 Apr 1) 103–108.
- X. Su, L. Lfiao, Y. Shuai, H. Jfing, S. Lfui, H. Zhou, et al., MiR-26a functions oppositely in osteogenic differentiation of BMSCs and ADSCs depending on distinct activation and roles of Wnt and BMP signalling pathway, *Cell Death Dis.* 6 (8) (2015 Aug 6).
- Y. Ili, L. Fan, J. Hu, L. Zhang, L. Lfiao, S. Lfui, et al., MiR-26a rescues bone regeneration deficiency of mesenchymal stem cells derived from osteoporotic mice, *Mol. Ther.* 23 (8) (2015 Aug 1) 1349–1357.
- M. Wu, G. Chen, Y.P. Ili, TGF- β and BMP signalling in osteoblast, skeletal development, and bone formation, *homeostasis and disease, Bone Res.* 4 (2016 Apr 26) 16009.
- A. Moustakas, S. Soucelynsky, C.H. Heidorn, Smad regulation in TGF- β signalling transduction, *J. Cell. Sci.* 114 (24) (2001 Dec 15) 4359–4369.
- E.G. Macfarlane, J. Haupt, H.C. Dietz, E.M. Shore, TGF- β family signalling in connective tissue and skeletal diseases, *Cold Spring Harb. Perspect. Biol.* 9 (11) (2017 Nov 1), a022269.
- H.N. Jo, H. Kang, A. Lee, J. Choi, W. Chang, M.S. Lee, et al., Endothelial miR-26a regulates VEGF-Nogo-B receptor-mediated angiogenesis, *BMB Rep.* 50 (7) (2017) 384.
- Y. Ili, L. Fan, S. Lfui, W. Lfui, H. Zhang, T. Zhou, et al., The promotion of bone regeneration through positive regulation of angiogenic-osteogenic coupling using microRNA-26a, *Biomaterials*. 34 (21) (2013 Jul 1) 5048–5058.
- S. Meyer, A.J. Weiland, H. Willehennegger, The treatment of infected non-union of fractures of long bones. Study of sixty-four cases with a five to twenty-one-year follow-up, *J. Bone Joint Surg.* 57 (6) (1975) 836–842.
- C. Lu, R. Marcucio, T. McElroy, Assessing angiogenesis during fracture healing, *Iowa Orthop. J.* 26 (2006) 17.
- R. Ili, J. Zhang, J. Shui, J. Yue, Y. Cui, Q. Ye, et al., An intelligent phase transformation system based on hydrophilic crystals for sequential biomolecule delivery to enhance bone regeneration, *J. Mater. Chem. B* 11 (13) (2023 Mar 30) 2946–2957.
- M. Sun, X. Zhou, L. Chen, S. Huang, V. Leung, N. Wu, et al., The regulatory roles of microRNAs in bone remodelling and perspectives as biomarkers in osteoporosis, *Biomater. Res. Int.* (2016) 1652417.
- L. Sun, Z. Ili, H. Xue, T. Ma, C. Ren, M. Lfui, et al., MiR-26a promotes fracture healing of nonunion rats possibly by targeting SOSTDC1 and further activating Wnt/ β -catenin signalling pathway, *Mol. Cell. Biochem.* 460 (1–2) (2019 Oct 1) 165–173.
- G. Cole, A.A. Afli, C.M. McCrudden, J.W. McBride, J. McCaffrey, T. Robson, et al., DNA vaccination for cervical cancer: strategic optimisation of RALA mediated gene delivery from a biodegradable microneedle system, *Eur. J. Pharm. Biopharm.* 127 (2018) 288–297.
- H.O. McCarthy, J. McCaffrey, C.M. McCrudden, A. Zhlobenko, A.A. Afli, J. W. McBride, et al., Development and characterization of self-assembling nanoparticles using a bioinspired amphiphilic peptide for gene delivery, *J. Control. Release* 189 (2014 Sep 10) 141–149.
- C.M. McCrudden, J.W. McBride, J. McCaffrey, E.M. McErlean, N.J. Dunne, V. L. Kett, et al., Gene therapy with RALA/fiNOS composite nanoparticles significantly enhances survival in a model of metastatic prostate cancer, *Cancer Nanotechnol.* 9 (1) (2018 Dec 1).
- M. McHale, O'Doherty, E.J. Mulfold, P. Chambers, S. Penflavafli, M. Zimfinska, M. J. Chaflanqu, H.M. Pauly, et al., Improving the intercellular uptake and osteogenic potency of calcium phosphate via nanocomplexation with the RALA peptide, *Nanomaterials* 10 (12) (2020 Dec 7) 2442.
- L.A. Bennie, J. Feng, C. Emmerson, W.B. Hyland, K.B. Matchett, H.O. McCarthy, et al., Formulating RALA/Na nanocomplexes to enhance nanoparticle internalisation efficiency, sensitising prostate tumour models to radiotherapy treatment, *J. Nanobiotechnol.* 19 (1) (2021 Sep 19) 1–13.
- V.K. Udhayakumar, A. De Beuckelaer, J. McCaffrey, C.M. McCrudden, J. L. Kirschman, D. Vanover, et al., Arginine-rich peptide-based mRNA nanocomplexes efficiently stimulate cytotoxic T cell immunity dependent on the amphiphilic organization of the peptide, *Adv. Healthc. Mater.* 6 (13) (2017) 1601412.
- G. Cole, A.A. Afli, E. McErlean, E.J. Mulfold, A. Short, C.M. McCrudden, et al., DNA vaccination via RALA nanoparticles in a microneedle delivery system induces a potent immune response against the endogenous prostate cancer stem cell antigen, *Acta Biomater.* 96 (2019 Sep 15) 480–490.

[45] L.P. Yan, I.M. Castano, R. Srividharan, D. Keflly, M. Lemofine, B.L. Cavanagh, et al., Collagen/GAG scaffolds activated by RALA-sf1/IMP-9 complexes with potential for improved diabetic foot ulcer healing, *Mater. Sci. Eng. C* 114 (2020 Sep 1), 111022.

[46] R. Bennett, A. Yakkundif, H.D. McKeen, L. McClellens, T.J. McKeogh, C. M. McCrudden, et al., RALA-mediated delivery of FKBPL nucleic acid therapeutics, *Nanomedicine* 10 (19) (2015 Oct 1) 2989–3001.

[47] R. McNally, A. Aflqudah, E.M. McErlean, C. Rennie, N. Morshed, A. Short, et al., Non-viral gene delivery utilizing RALA modulates sfl-1 secretion, important for preeclampsia, *Nanomedicine (London)* 16 (22) (2021 Sep 1) 1999–2012.

[48] C.M. McCrudden, J.W. McBride, J. McCaffrey, A.A. Afl, N.J. Dunne, V.L. Kett, et al., Systemic RALA/sf1NOS nanoparticles: a potent gene therapy for metastatic breast cancer coupled as a biomarker of treatment, *Mol. Ther. Nucl. Acids* 6 (2017 Mar 17) 249–258.

[49] M. Zimfinska, J.J. Wiflson, E. McErlean, N. Dunne, H.O. McCarthy, Synthesis and evaluation of a thermoresponsive degradable chitosan-grafted PNIPAAm hydrogel as a 'smart' gene delivery system, *Materials (Basel)* 13 (11) (2020 Jun 2) 2530.

[50] N. Wong, X. Wang, miRDB: an online resource for microRNA target prediction and functional annotations, *Nucleic Acids Res.* 43 (Database issue) (2015 Jan 28) D146–D152.

[51] C.H. Chou, N.W. Chang, S. Shrestha, Hsu S. Da, Y.L. Ilin, W.H. Lee, et al., miRTarBase 2016: updates to the experimentally validated miRNA-target interactions database, *Nucleic Acids Res.* 44 (D1) (2016 Jan 4) D239–D247.

[52] J. Schindlifl, I. Arganda-Carreras, E. Frise, V. Kaynig, M. Longair, T. Pfei, et al., Fijit: an open-source platform for bioinformatic image analysis, *Nat. Methods* 9 (7) (2012 Jul) 676–682.

[53] H. Youn, J.K. Chung, Modified mRNA as an alternative to plasmid DNA (pDNA) for transcript replacement and vaccination therapy, *Expert. Opin. Biolog. Ther.* 15 (9) (2015 Sep 9) 1337.

[54] P.P. Spicer, J.D. Kretlow, S. Young, J.A. Jansen, F.K. Kasper, A.G. Mifikos, Evaluation of bone regeneration using the rat critical size calvarial defect, *Nat. Protoc.* 7 (10) (2012 Sep 6) 1918–1929.

[55] P.P. Spicer, J.D. Kretlow, S. Young, J.A. Jansen, F.K. Kasper, A.G. Mifikos, Evaluation of bone regeneration using the rat critical size calvarial defect, *Nat. Protoc.* 7 (10) (2012 Oct) 1918–1929, 2012/09/27.

[56] K.S. Klim, J.Y. Lee, Y.M. Kang, E.S. Klim, G.H. Klim, S.D. Rhee, et al., Small intestine submucosa sponge for in vivo support of tissue-engineered bone formation in the presence of rat bone marrow stem cells, *Biomaterials* 31 (6) (2010 Feb) 1104–1113.

[57] Y. Ili, L. Fan, S. Iliu, W. Iliu, H. Zhang, T. Zhou, et al., The promotion of bone regeneration through positive regulation of angiogenic-osteogenic coupling using microRNA-26a, *Biomaterials* 34 (21) (2013) 5048–5058.

[58] A. Quilliet, C. Saad, G. Ferry, Y. Anouar, N. Vergne, T. Lecroq, et al., Improving bioinformatics prediction of microRNA targets by ranks aggregation, *Front. Genet.* 10 (2020 Jan 28) 1330.

[59] V. Agarwall, G.W. Belfi, J.W. Nam, D.P. Bartel, Predicting effective microRNA target sites in mammalian mRNAs, *Elife* 4 (AUGUST2015) (2015 Aug 12).

[60] J. Rejman, V. Oberle, I.S. Zuhorn, D. Hoekstra, Size-dependent internalization of particles via the pathways of clathrin- and caveolae-mediated endocytosis, *Biochem. J.* 377 (Pt 1) (2004 Jan 1) 159.

[61] E.M. McErlean, C.M. McCrudden, J.W. McBride, G. Cofle, V.L. Kett, T. Robson, et al., Rational design and characterization of an amphiphatic cell penetrating peptide for non-viral gene delivery, *Int. J. Pharm.* 596 (2021 Mar 1), 120223.

[62] P. Forozandeh, A.A. Aziz, Insight into Celluloflular Uptake and Intracellular Trafficking of Nanoparticles. Vol. 13, Nanoscale Research Letters, Springer New York LLC, 2018.

[63] S. Yao, Y. Xu, Y. Zhou, C. Shao, Z. Iliu, B. Ilin, et al., Cellulose phosphate nanocluster-loaded injectable hydrogel for bone regeneration, *ACS Appl. Bio Mater.* 2 (10) (2019 Oct 21) 4408–4417.

[64] M. Arnold, S. Zhao, S. Ma, F. Giuffrè, U. Hansen, J.P. Cob, et al., Microindentation – a tool for measuring critical bone stiffness?: a systematic review, *Bone Joint Res.* 6 (9) (2017 Sep 1) 542.

[65] E.K. Tsekoura, K.C. Remant Bahadur, H. Usludag, Biomaterials to facilitate delivery of RNA agents in bone regeneration and repair, *ACS Biomater. Sci. Eng.* 3 (7) (2017 Jul 10) 1195–1206.

[66] X. Zhang, Y. Ili, Y.E. Chen, J. Chen, P.X. Ma, Cell-free 3D scaffold with two-stage delivery of miRNA-26a to regenerate critical-sized bone defects, *Nat. Commun.* 7 (2016 Jan 14) 10376.

[67] M.F. Ye, D. Ilin, W.J. Ili, H.P. Xu, J. Zhang, MiR-26a-5p serves as an oncogenic microRNA in non-small cell lung cancer by targeting FAF1, *Cancer Manag. Res.* 12 (2020) 7131–7142.

[68] B. Chen, Deng Y. Nan, X. Wang, Z. Xia, Y. He, P. Zhang, et al., miR-26a enhances colorectal cancer cell growth by targeting RREB1 deacetylation to activate AKT-mediated glycolysis, *Cancer Lett.* (521) (2021 Nov 28) 1–13.

[69] H. Wang, Z. Hu, L. Chen, Enhanced plasma miR-26a-5p promotes the progression of bladder cancer via targeting PTEN, *Oncol. Lett.* 16 (4) (2018 Oct 1) 4223–4228.

[70] B. Iclif, A.K.M. Wara, J. Mosleh, X. Sun, E. Pflow, M. Cahifl, et al., MicroRNA-26a regulates pathophysiological and physiological angiogenesis by targeting BMP/SMAD1 signaling, *Circ. Res.* 113 (11) (2013 Nov 8) 1231–1241.

[71] Y. Ili, D. Guo, Y. Zhao, M. Ren, G. Lu, Y. Wang, et al., Long non-coding RNA SNHG5 promotes human hepatocelluloflular carcinoma progression by regulating miR-26a-5p/GSK3β signaling pathway, *Circ. Death.* 9 (9) (2018 Aug 30) 1–15.

[72] J. McCaffrey, C.M. McCrudden, A.A. Afl, A.S. Massey, J.W. McBride, M.T. C. McCrudden, et al., Transcending epithelial and intracellular biological barriers: a prototype DNA delivery device, *J. Control. Release* 226 (2016 Mar 28) 238–247.

[73] C.L. Da Sifiva, C. Madefira, R.D. Mendes, S.C. Ribeiro, J.S. Boura, M.R. Afres-Barros, et al., Nonviral gene delivery to mesenchymal stem cells using cationic liposomes for gene and cell therapy, *J. Biomed. Biotechnol.* 2010 (2010).

[74] W.Y. Cheung, O. Hovey, J.M. Gobin, G. Muradfa, J. Mehic, C. Westwood, et al., Efficient nonviral transfection of human bone marrow mesenchymal stromal cells shown using placental growth factor overexpression, *Stem Cells Int.* 2018 (2018 Dec 24) 1310904.

[75] S. Mahati, X. Fu, X. Ma, H. Zhang, L. Xfiao, Delivery of miR-26a using an exosomes-based nanosystem inhibits proliferation of hepatocelluloflular carcinoma, *Front. Mol. Biosci.* 8 (2021 Sep 6) 847.

[76] Y. Cufi, Y. Guo, L. Kong, J. Shfi, P. Iliu, R. Ili, et al., A bone-targeted engineered exosome platform delivering siRNA to treat osteoporosis, *Bioact. Mater.* 10 (2022 Apr 1) 207–221.

[77] Y. Cufi, Z. Ili, Y. Guo, X. Qfi, Y. Yang, X. Jfia, et al., Bioinspired nanovesicles convert the skeletal endothelial-associated secretory phenotype to treat osteoporosis, *ACS Nano* 16 (7) (2022 Jul 26) 11076–11091.

[78] Y. Sasano, J.X. Zhu, S. Kamakura, S. Kusunokfi, I. Mifizoguchfi, M. Kagayama, Expression of major bone extracellular matrix proteins during embryonic osteogenesis in rat mandibles, *Anat. Embryol. (Berl)* 202 (1) (2000) 31–37.

[79] S. Shfi, M. Kifir, A.J. Kahn, The role of type I collagen in the regulation of the osteoblast phenotype, *J. Bone Miner. Res.* 11 (8) (1996) 1139–1145.

[80] Y. Ili, L. Fan, S. Iliu, W. Iliu, H. Zhang, T. Zhou, et al., The promotion of bone regeneration through positive regulation of angiogenic-osteogenic coupling using microRNA-26a, *Biomaterials* 34 (21) (2013 Jul) 5048–5058.

[81] Z. Wang, Q. Xfie, Z. Yu, H. Zhou, Y. Huang, X. Bf, et al., A regulatory loop containing miR-26a, GSK3β and C/EBPα regulates the osteogenesis of human adipose-derived mesenchymal stem cells, *Sci. Rep.* 5 (1) (2015 Oct 15) 1–18.

[82] L.F. Fröhlich, MicroRNAs at the interface between osteogenesis and angiogenesis as targets for bone regeneration, *Elife* 8 (2) (2019 Feb 3) 121.

[83] J. Street, D. Wfnter, J.H. Wang, A. Wakaf, A. McGuffiness, H.P. Redmond, Is human fracture hematoma inherently angiogenic? *Orthop. Relat. Res.* 378 (2000) 224–237.

[84] T. Furumatsu, Z.N. Shen, A. Kawafi, K. Nifishida, H. Manabe, T. Oohashfi, et al., Vascular endothelial growth factor pifcifipally acts as the mafin angiogenic factor in the early stage of human osteoblastogenesis, *J. Biochem.* 133 (5) (2003 May 1) 633–639.

[85] A.D. Kaneflopoulos, P.N. Soucacos, Management of nonunion with distraction osteogenesis, *Injury* 37 (Suppl. 1) (2006 Apr) 1.

[86] R. McBeath, D.M. Pifrone, C.M. Neflson, K. Bhadriraju, C.S. Chen, Cell shape, cytoskeletal tension, and RhoA regulate stem cell lineage commitment, *Dev. Cell* 6 (4) (2004 Apr) 483–495.

[87] F. Hefitz, M.C. Morris, G. Difvita, Twenty years of cell-penetrating peptides: from molecular mechanisms to therapeutics, *Br. J. Pharmacol.* 157 (2) (2009 May) 195–206.

[88] Z. Iliu, H. Chang, Y. Hou, Y. Wang, Z. Zhou, M. Wang, et al., Lentivirus-mediated microRNA-26a overexpression in bone mesenchymal stem cells facilitates bone regeneration in bone defects of calvaria in mice, *Mol. Med. Rep.* 18 (6) (2018 Dec 1) 5317–5326.

[89] Y. Ili, L. Fan, J. Hu, L. Zhang, L. Lfiao, S. Iliu, et al., MiR-26a rescues bone regeneration deficiency of mesenchymal stem cells derived from osteoporotic mice, *Mol. Ther.* 23 (8) (2015 Aug 1) 1349–1357.

[90] J. Gorecka, V. Kostuk, A. Fereydoonfi, L. Gonzalez, J. Luo, B. Dash, et al., The potential and limitations of induced pluripotent stem cells to achieve wound healing, *Stem Cell Res Ther* 10 (1) (2019 Mar 12) 1–10.

[91] Y. Ili, L. Fan, J. Hu, L. Zhang, L. Lfiao, S. Iliu, et al., MiR-26a rescues bone regeneration deficiency of mesenchymal stem cells derived from osteoporotic mice, *Mol. Ther.* 23 (8) (2015 Aug) 1349–1357, 2015/06/08.

[92] R. Ili, H. Wang, J.V. John, H. Song, M.J. Teusink, J. Xfie, 3D hybrid nanofiber aerogels combining with nanoparticles made of a biodegradable and targeting polycation and MiR-26a for bone repair, *Adv. Funct. Mater.* 30 (49) (2020 Dec 1) 2005531, 2020/09/09.